

Submitted by
Julian Hofer, B.Sc.

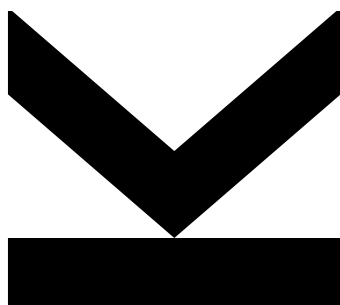
Submitted at
Institute of Semiconductor and Solid State Physics

Supervisor
Prof. Dr. Armando Rastelli

Co-Supervisor
DI Christian Schimpf

September 2019

Advanced excitation and spectroscopy schemes of single quantum dots



Master Thesis
to obtain the academic degree of
Diplom-Ingenieur
in the Master's Program
Technische Physik

Eidesstattliche Erklärung

Ich erkläre an Eides statt, dass ich die vorliegende Masterarbeit selbstständig und ohne fremde Hilfe verfasst, andere als die angegebenen Quellen und Hilfsmittel nicht benutzt bzw. die wörtlich oder sinngemäß entnommenen Stellen als solche kenntlich gemacht habe. Die vorliegende Masterarbeit ist mit dem elektronisch übermittelten Textdokument identisch.

Datum

Unterschrift

Acknowledgement

First I would like to thank the head of our group Armando Rastelli for offering me this position and for making sure to always have an open ear, no matter how busy he was at the moment.

I would also like to thank Christian Schimpf for taking the role as my unofficial supervisor. I cannot think of anyone who would have fulfilled it better than him.

Thanks belongs to most of my group members, but I want to especially highlight Marcus Reindl and Daniel Huber who granted me the biggest support.

Further, I would like to thank Susanne Schwind for solving every administrative issue that came along my way.

Last but not least, I would like to thank my parents for supporting every goal I have ever pursued in my life and of course Sabrina for more reasons than I could ever possibly list.¹

¹This document is set in Palatino, compiled with pdfL^AT_EX2e and Biber. The L^AT_EX template from Karl Voit is based on KOMA script and can be found online: <https://github.com/novoid/LaTeX-KOMA-template>

Zusammenfassung

In dieser Arbeit wird die Anregung von Quantenpunkten mittels Adiabatic Rapid Passage und die Spektroskopie der Quantenpunktemission mit einem Scanning Fabry Pérot Interferometer (FPI) diskutiert. Zunächst wird die Verwendung von GaAs-Quantenpunkten als Quelle für Einzelphotonen und verschränkten Photonenpaare motiviert und Details zu deren Herstellung und optischen Eigenschaften vorgestellt. Der für die Messungen verwendete optische Aufbau wird skizziert und es werden Methoden wie die Mikro-Photolumineszenz erläutert. Anschließend wird die Verwendung von Adiabatic Rapid Passage zur Erzeugung verschränkter Photonen motiviert und deren Implementierung mit frequenz-gechirpten Pulsen erläutert. Die Theorie hinter dem Chirp wird vorgestellt und führt zur Beschreibung einer Anordnung, mit der der Chirp eines Laserstrahls deterministisch eingestellt werden kann. Der gechirpte Strahl wurde mit einem interferometrischen Autokorrelator gemessen und der numerische Filter MOSAIC wurde verwendet, um den Chirp-Parameter aus diesen Messungen zu extrahieren.

Schließlich werden Scanning FPIs als Werkzeuge zum Auflösen feiner Merkmale der Quantenpunktemission vorgestellt. Der Leser / die Leserin wird durch die Theorie der Gaußschen Strahlen und die Berechnung allgemeiner FPI-Eigenschaften geführt, die von Resonatorverlusten bis zu ihren Transmissionsspektrum reichen. Es werden Methoden zur Unterdrückung höherer Gauß-Modi vorgestellt und Simulationen zur Größenbestimmung der Bauteile des FPIs gezeigt. Abschließend werden Messungen mit schnellen Fotodioden und CCD-Sensoren vorgestellt und damit die Eignung zum Auflösen der Feinstruktur eines GaAs-Quantenpunktes gezeigt.

Abstract

In this thesis excitation of quantum dots via adiabatic rapid passage and spectroscopy of quantum dot emission with a scanning Fabry Pérot interferometer (FPI) are discussed. First, the use of GaAs quantum dots as sources of (entangled) single photons is motivated and details of their fabrication and optical properties are presented. The optical setup used for the measurements is sketched and methods like micro photo-luminescence are explained. Subsequently, the use of adiabatic rapid passage for entangled photon generation is motivated and its implementation with frequency-chirped pulses is explained. The theory behind the chirp is presented, leading to the description of a setup used to deterministically adjust the chirp of a laser beam. The chirped beam was measured with an interferometric autocorrelator and the numerical filter MOSAIC was used to extract the chirp parameter from these measurements.

Finally, scanning FPIs as tools to resolve fine features of quantum dot emission are presented. The reader is guided through the theory of Gaussian beams and the calculation of common FPI properties, ranging from resonator losses to its transmission spectrum. Methods to suppress higher Gauss modes are presented and simulations are shown used to size the FPI. Finally, measurements with fast photodiodes and CCD sensors are presented and with them the suitability for resolving the fine structure of a GaAs quantum dot is shown.

Contents

Zusammenfassung

Abstract

1. Introduction	1
2. Gallium arsenide quantum dots	3
2.1. Fabrication and optical properties	3
2.2. Fine structure splitting	6
2.3. Zero-phonon line and phonon sideband	8
2.4. Optical excitation of a quantum dot	11
2.5. Single photon emission	12
3. Methods	15
3.1. Optical setup	15
3.2. Pulse shaper	16
3.3. Micro photo-luminescence	16
4. Entangled photon generation using adiabatic rapid passage with frequency-chirped pulses	19
4.1. Introduction and motivation	19
4.2. Chirp	19
4.3. Measuring the chirp with interferometric autocorrelation	22
4.4. Deterministically adjusting the chirp with a pulse expander	25
4.5. Adiabatic rapid passage	26
4.6. Measurements and discussion	28
5. Planning and building a Fabry-Pérot interferometer	31
5.1. Introduction and motivation	31

5.2.	Transverse modes of electromagnetic radiation	31
5.2.1.	Gaussian beam	31
5.2.2.	Hermite–Gaussian modes	34
5.3.	Fundamentals of Fabry-Pérot interferometers	35
5.3.1.	Resonator losses	35
5.3.2.	Resonance frequencies, free spectral range and spectral line shapes	36
5.3.3.	Airy distribution of Fabry-Pérot interferometers	37
5.3.4.	Airy linewidth and finesse	38
5.3.5.	Mode matching and spatial filtering	40
5.3.6.	Confocal setup	43
5.4.	Simulation	44
5.5.	Setup and testing	47
5.5.1.	Scanning mode with fast photodiodes	49
5.5.2.	Scanning mode with CCD	50
5.6.	Measurements and discussion	51
6.	Summary and outlook	55
A.	Acronyms	59
Bibliography		61

List of Figures

2.1.	Droplet etched GaAs quantum dots.	4
2.2.	Biexciton-exciton decay cascade in a QD.	5
2.3.	Fine structure splitting in a GaAs quantum dot.	7
2.4.	Absorption line shape of an electronic excitation.	8
2.5.	Zero-phonon line and phonon sideband. [28]	9
2.6.	Optical pumping of a QD by (a) above-band excitation and (b) resonant excitation [18]	11
2.7.	Resonant two photon excitation [19]	12
2.8.	Hanbury-Brown-Twiss HBT experiment [19]	13
3.1.	Complete experimental setup	15
3.2.	Laser beam of different spot sizes illuminating quantum dots [37].	17
4.1.	A chirped sinusoidal wave which increases in frequency over time.	20
4.2.	Electric field E of Gaussian laser pulse of pulse duration $\tau_0 = 0.5 \text{ ps}$ for chirp of (a) $\alpha = 0.1 \text{ ps}^2$ and (b) $\alpha = 0.5 \text{ ps}^2$	21
4.3.	Schematics of an interferometric autocorrelator	22
4.4.	Intensity of IAC of a Gaussian laser pulse of pulse duration $\tau_0 = 0.5 \text{ ps}$ without applied MOSAIC filter for chirp of (a) $\alpha = 0.1 \text{ ps}^2$ and (b) $\alpha = 0.5 \text{ ps}^2$	22
4.5.	Intensity of IAC of a Gaussian laser pulse of pulse duration $\tau_0 = 0.5 \text{ ps}$ for chirp of (a) $\alpha = 0.1 \text{ ps}^2$ and (b) $\alpha = 0.5 \text{ ps}^2$	23
4.6.	Intensity of IAC of a Gaussian laser pulse of pulse duration $\tau_0 = 0.5 \text{ ps}$ with applied MOSAIC filter for chirp of (a) $\alpha = 0.1 \text{ ps}^2$ and (b) $\alpha = 0.5 \text{ ps}^2$. The orange dots are results of a numerical peak finder algorithm, executed in order to find local minima.	24
4.7.	Intensity of IAC of a Gaussian laser pulse of pulse duration $\tau_0 = 0.5 \text{ ps}$ with applied MOSAIC filter and fitted α -values.	25
4.8.	Scheme of a folded pulse expander as described by Martinez [43].	25
4.9.	Influence of group velocity dispersion for example inside a fiber on a Gaussian pulse [44]	26

4.10. Final biexciton occupation after chirped Gaussian pulse of pulse duration $\tau_0 = 2 \text{ ps}$	27
4.11. Measured IAC of Ti:Sa Laser without (a) and with (b) pulse expander before the autocorrelator.	28
4.12. Measured IAC of Ti:Sa Laser with applied MOSAIC filter without (a) and with (b) pulse expander before the autocorrelator.	29
5.1. A Gaussian beam near its beam waist.	33
5.2. Gaussian modes higher order of a simple Ti-sapphire laser	35
5.3. Fabry P��rot interferometer with electric field mirror reflectivities r_1 and r_2	37
5.4. Airy distribution A'_{trans}	38
5.5. Demonstration of the physical meaning of the Airy finesse F_{Airy}	39
5.6. Incident monochromatic beam of light exciting transverse mode m, n of a resonator [50]	40
5.7. Mode matching of an Gaussian beam into a Fabry P��rot interferometer.	41
5.8. Spatial filtering of Gauss modes.	43
5.9. Simulated exciton emission of a GaAs quantum dot	45
5.10. The exciton emission $\Phi_{dot}(E)$ (red) compared to the transmission of the FPI modes A'_{trans} (blue) of a FPI with a mirror distance l suitable to resolve either (a) the ZPL or (b) the PSB.	45
5.11. Transmissions of the FPI modes A'_{trans} (blue) for different mirror distances $l - m \cdot \Delta l$ with $m \in \mathbb{N}$ compared to the exciton emission $\Phi_{dot}(E)$ (red).	46
5.12. Output-photon-flux of the scanning FPI $\Phi_{FPI}(E)$ (blue) compared to the exciton emission $\Phi_{dot}(E)$ (red) for (a) ZPl and (b) PSB.	46
5.13. In (a) the shifted output-photon-flux of the scanning FPI $\bar{\Phi}_{FPI}(E)$ (blue) compared to the exciton emission $\Phi_{dot}(E)$ (red) is displayed. In (b) the absolute difference between those two $ \bar{\Phi}_{FPI}(E) - \Phi_{dot}(E) $ (light blue) is additionally shown.	47
5.14. Comparison between two setups where one uses bigger, planar mirrors and one uses smaller, planar-convex mirrors	48
5.15. Top view of FPI and casing.	49
5.16. Live avalanche photodiode setup using a function generator driving the piezo actuator of the FPI and the sync input of the correlation hardware. APDs are used because of their speed, allowing to live-adjusting the FPI-parameters.	49
5.17. Measurement of scanning FPI with APDs. The scanning frequency is 5 Hz and the range is 1 μm . The measured finesse is ≈ 5 and the free spectral range corresponds to 280 nm.	50
5.18. Scanning Fabry P��rot interferometer with CCD	51

List of Figures

5.19. Aligning the Fabry Pérot interferometer	51
5.20. Transmission measurement of FPI with ground mirror distance $l \approx 2$ mm and HeNe laser. (a) was aligned without spatial filtering with a pinhole and (b) involved a pinhole.	52
5.21. Polarization map of exciton-groundstate decay emission of QD in sample AS208. The peak to peak amplitude corresponds to the fine structure splitting.	53
5.22. Fine-structure measurement of exciton decay emission of a QD in sample AS208. It is measured by passing the QD emission through a FPI and sweeping the mirror distance. The ground mirror distance is $l \approx 2$ mm.	53

1. Introduction

In the past century, technology was transformed by the first quantum revolution. Scientists and engineers all around the world utilized certain features of quantum mechanics such as energy quantization and wave-particle duality to create devices which are nowadays a fixed part of everyone's life. These technologies, ranging from semiconductor devices to LEDs and lasers, became high-performance components which drive modern information processing and global communication networks. The second quantum revolution to come shall make use of superposition and entanglement [1][2].

Entanglement is already the basis of many experiments in quantum computation and its distinct properties can be used for quantum cryptography protocols as well [3]. It describes a physical phenomenon involving two or more particles whose quantum states cannot be described independently from each other. Entanglement is especially useful when the entangled particles are photons, as these can be transported over long distances with optical fibres and are therefore ideal to build up quantum networks [4]. Quantum key distribution (QKD) under the E91 protocol [5] can use the quantum network to exchange entangled photons and then generate a shared encryption key. Since the photons are entangled, the key can be generated in a way which prevents that potential eavesdropping could go unnoticed. The key is then used to encrypt the data by one party, the encrypted data is transmitted via classical channels and afterwards it is decrypted with the very same key by the other party. The E91 protocol with its use of entanglement has the advantage that it allows to detect eavesdropping even with lossy channels, which is a feature other implementations of QKD cannot necessarily provide.

In order to use entangled photons for QKD several problems have to be solved first. Fibre and free space channels suffer from decoherence and optical losses [6]. This reduces the amount of photons to a point where they are unsuitable for secure quantum protocols and therefore limits the maximal communication distance. Usually classical amplifiers would be used to counteract transmission losses, however this does not work with quantum states because of the no cloning theorem [7]. In order to solve this problems, multiple teams are currently working on quantum repeaters [8][9][10].

1. Introduction

The E91 protocol and quantum repeaters both require sources of single entangled photons. Two prominent sources are parametric down conversion crystals [11] and single atoms [12][13]. However the number of entangled photon pairs with parametric down conversion is probabilistic, which means that the number of entangled photon pairs emitted per excitation pulse is statistically distributed. Single atoms offer sharp electronic transitions, are free from charge fluctuations and are energetically isolated. Nowadays advanced techniques [14] are used in order to operate with single-atom-based sources, but their arrangements are bulky and their dynamics are relatively low, leading to slow operation rates.

Quantum dots (QD) provide an alternative source of single entangled photons. QD sources are in principle deterministic, with a state preparation probability of approximately 90 % and a current maximum of 85 % extraction efficiency [15]. Under several conditions, they also emit maximally one photon pair per excitation cycle [16]. With this motivation in mind, droplet-etched GaAs quantum dots as potential sources are investigated in chapter 2, as they are quasi strain-free, of high symmetry and exhibit low values of fine structure splitting (FSS). Optical experiments on QDs require several methods which are introduced in chapter 3. Usually, entangled photon pairs are obtained by exciting the biexciton state via resonant two-photon excitation. However, resonant two-photon excitation typically requires precise control of the intensity of the exciting field in order to invert the quantum dot from the ground state to the biexciton state [17]. Adiabatic rapid passage and alternative excitation schemes using frequency-chirped pulses do not suffer from this requirement, which motivates their discussion in chapter 4.

Quantum repeaters rely on indistinguishable photons, which means that they match in all possible parameters and degrees of freedom. Indistinguishability could be estimated by analysing the time-averaged line shape [8]. However, fine features of the emission spectrum are not resolvable with a standard CCD-based spectrometer alone. A Fabry Pérot interferometer (FPI) can be used to resolve QD emission spectra while still using the same spectrometer as an accurate power meter. A FPI transmits signals of certain frequencies and these frequencies can be adjusted in order to scan through the ranges of interest. QD emission is sent through the scanning interferometer and its output power is then recorded with the CCD allowing to reassemble the complete spectrum. Chapter 5 describes the efforts to build up a scanning FPI to do exactly that. Chapter 6 summarises the work discussed in this thesis and gives a brief outlook to the next steps.

2. Gallium arsenide quantum dots

2.1. Fabrication and optical properties

Quantum dots (QD) are nanostructures which confine the motion of electrons and holes in all three spatial dimensions. Confinement results in discrete energy levels, which is why QDs are sometimes referred to as *artificial atoms*. The discussion in this section is based on the PhD thesis of Huber [18] and on the master's thesis of Schimpf [19].

The Gallium arsenide QDs investigated within this master's thesis are grown by molecular beam epitaxy (MBE) with the self-assembled nanodrill technology described in the work of Wang et al. [20]. As displayed in figure 2.1a the Al forms droplets on $\text{Al}_{0.4}\text{Ga}_{0.6}\text{As}$ after evaporation. The Al reacts with $\text{Al}_{0.4}\text{Ga}_{0.6}\text{As}$, etching nanoholes into the surface. Under ideal conditions, these nanoholes are highly symmetric, resulting into QDs with high in-plane symmetry, as can be seen in figure 2.1b. The next step is the annealing process, in which GaAs is deposited to fill the nanoholes. The QD is finalized by capping the layer with $\text{Al}_{0.4}\text{Ga}_{0.6}\text{As}$ acting as top barrier.

Compared to the band gap of the host material $\text{Al}_{0.4}\text{Ga}_{0.6}\text{As}$ of 1.92 eV at room temperature, the core of the QD, GaAs has a band gap of only 1.42 eV at room temperature. The energy difference between the bandgaps and the type-I band alignment depicted in figure 2.1c are responsible for the 3D confinement, leading to discrete energy levels. Inside of the QD, optical transitions are possible. Transitions between the first energy level in the conduction band (CB) and the valence band (VB), often called the s-shell, are here of special interest. The carriers involved are the electrons (e^-) and the holes (h^+) left behind. These are fermions and therefore only up to two of them can, in accordance with Pauli's exclusion principle, occupy a single energy state. Electrons and holes are strongly localized inside the QD by the confinement potential and influence each other by Coulomb attraction and exchange interaction [21]. This leads to multi-particle complexes with the most fundamental being the exciton (X), a quasi-particle

2. Gallium arsenide quantum dots

consisting of an electron and a hole, bound by Coulomb interaction. Fully occupied s-shells form the biexciton (XX), consisting of two electrons and two holes of opposite spins.

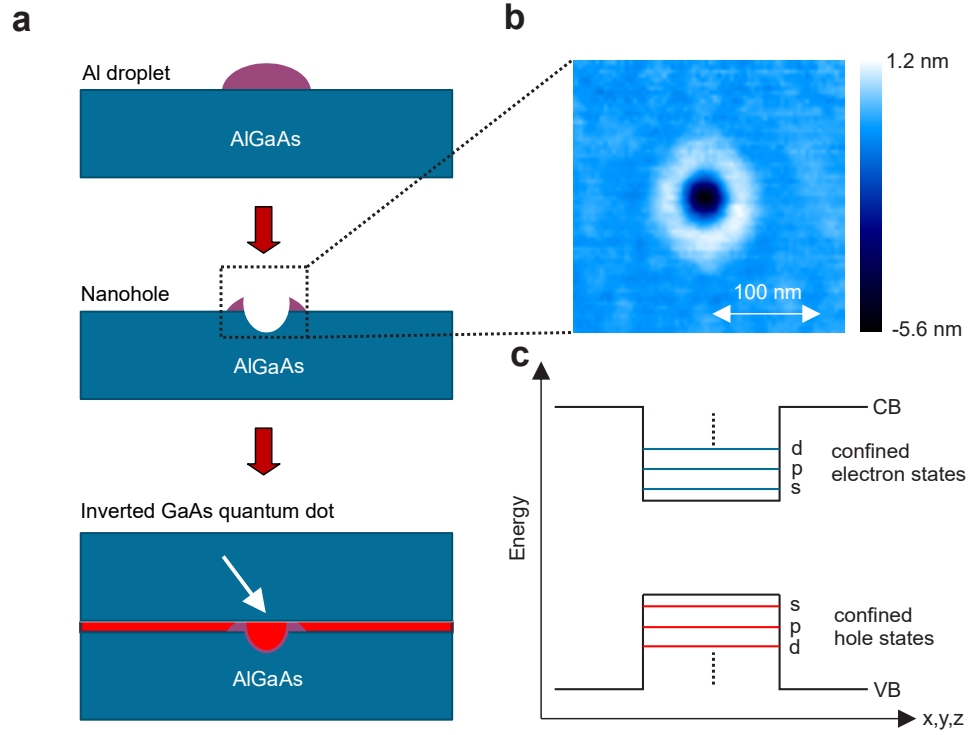


Figure 2.1.: (a) The growth process of a GaAs quantum dot by MBE.

(b) Atomic force microscopy (AFM) image of the nanohole before it is filled with GaAs.

(c) Conduction band (CB) and valence band (VB) of an optically active QD. [18]

In a QD, polarization-entangled photon pairs can be generated via a biexciton-exciton decay cascade [22], illustrated in figure 2.2. The $|XX\rangle$ state forms a full shell, which means that the total angular momentum projection along the quantization axis of the XX complex sums up to $M = 0$. If the QD is radially symmetric, M is preserved and $|M\rangle$ are eigenstates of the system. After exciting the QD into the $|XX\rangle$ state (e.g. by optical pumping) it decays by spontaneous recombination of an electron-hole-pair accompanied by the emission of a single photon into the $|X\rangle$ state.

The two dipole-allowed radiative transitions lead to only two possible angular momentum states of the exciton:

- $| -1 \rangle$ under emission of a right-circularly-polarized photon $| R_{XX} \rangle$
- $| +1 \rangle$ under emission of a left-circularly-polarized photon $| L_{XX} \rangle$

$| -1 \rangle$ and $| +1 \rangle$ are degenerated in energy and decay into the groundstate $| G \rangle$ under emission of $| L_X \rangle$ and $| R_X \rangle$, respectively. The resulting two-photon state is then described by

$$| \psi^+ \rangle = \frac{1}{\sqrt{2}} (| L_{XX} \rangle | R_X \rangle + | R_{XX} \rangle | L_X \rangle) \quad (2.1)$$

which is one of the four Bell states, representing the maximally entangled two-particle states.

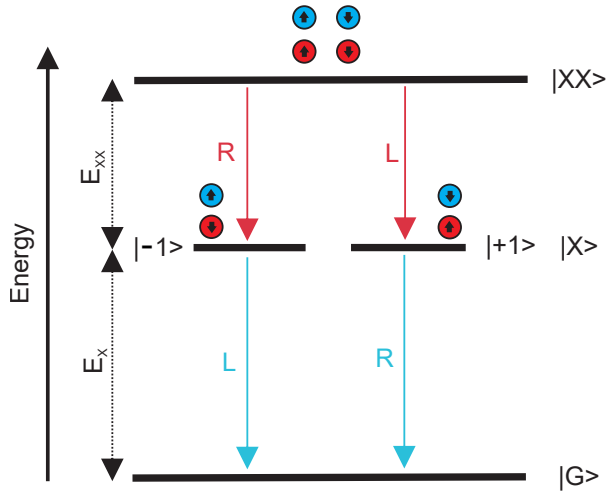


Figure 2.2.: Biexciton-exciton decay cascade in a QD. The $| XX \rangle$ state can decay via two paths under the emission of a right (left) polarized photon into one of two energetically degenerated $| X \rangle$ states. The $| X \rangle$ state then decays into the ground state $| G \rangle$ under the emission of a left (right) polarized photon. [18]

In order to calculate the life time of the X and XX states and the respective spectral distribution of the emission, the radiative transition rate Γ between quantum mechanical states has to be derived. Γ describes the transition probability per unit time from an initial state $| i \rangle$ to a final state $| f \rangle$ and can be calculated by Fermi's golden rule if the transition occurs because of a weak perturbation. In the dipole approximation it depends on

$$\Gamma \propto |\langle f | \mathbf{e} \cdot \hat{\mathbf{p}} | i \rangle|^2 \delta(E_i - E_f - E_P) \quad (2.2)$$

with \mathbf{e} the unit polarisation vector of the emission, $\hat{\mathbf{p}}$ the momentum operator of the electron and E_f , E_i and E_P the energies of the final state, of the initial state and of the emitted photon respectively. The

2. Gallium arsenide quantum dots

rate equation for the population of the initial state can then be expressed as

$$\frac{dN_i(t)}{dt} = -\Gamma N_i(t) \quad (2.3)$$

which results into exponential decay as solution

$$N_i(t) = N_i(0)e^{-t/\tau} \quad (2.4)$$

where the lifetime of the initial state is defined as $\tau = 1/\Gamma$.

This can be applied for the X and XX states with decay constants τ_ν and intensity for the emitted light $I_\nu(t)$, where $\nu \in \{X, XX\}$. The Fourier transform of the electric field yields a Cauchy distribution

$$I_\nu(\omega) = \frac{1}{2\pi\tau_\nu} \frac{1}{(\omega - \omega_\nu)^2 + \left(\frac{1}{2\tau_\nu}\right)^2} \quad (2.5)$$

with $\omega_\nu = e_\nu/\hbar$ denoting its center frequency.

2.2. Fine structure splitting

The FSS in a QD describes the energy splitting between the two possible bright $|X\rangle$ states, which originates from the exchange interaction between electrons and holes. [23]. The electron-hole exchange Hamiltonian is described by

$$\mathcal{H}_{ex} = - \sum_{i=x,y,z} a_i J_{h,i} S_{e_i} + b_i J_{h,i}^3 S_{e_i} \quad (2.6)$$

with a_i and b_i the spin-coupling constants, $J_{h,i}$ the holes' and S_{e_i} the electrons' total angular momentum. The z-direction is assigned as the crystal growth direction and the bright X states are defined by the projections of J_h and S_e to the z-axis, so that $|+1\rangle = |+\frac{3}{2}, -\frac{1}{2}\rangle$ and $| -1\rangle = |-\frac{3}{2}, +\frac{1}{2}\rangle$. The Hamiltonian of equation (2.6) can then be described in the bases $\{|+1\rangle, |-1\rangle\}$

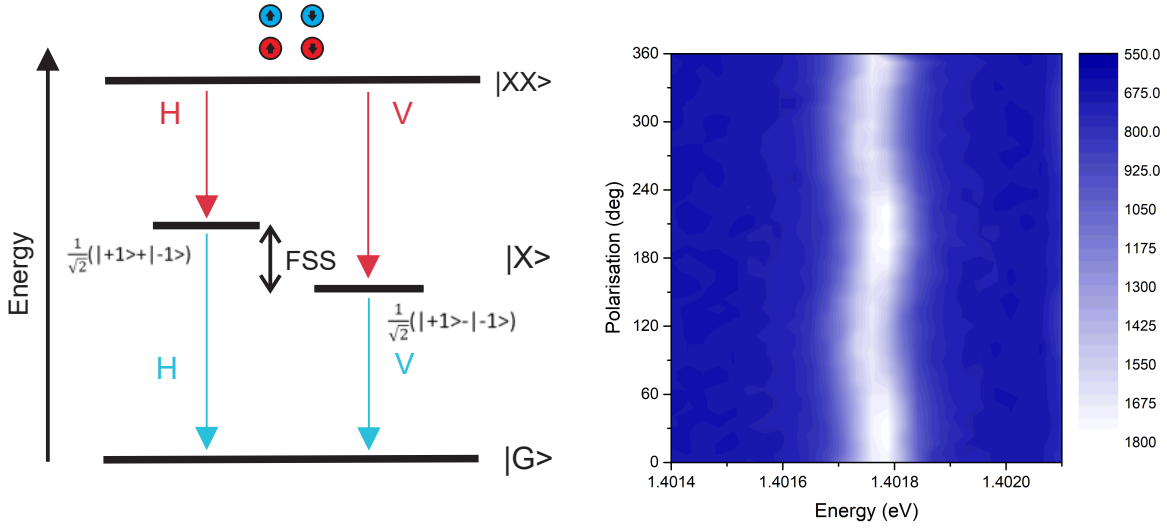
$$\mathcal{H}_{ex} = \begin{pmatrix} \langle +1|\mathcal{H}_{ex}|+1\rangle & \langle +1|\mathcal{H}_{ex}| -1\rangle \\ \langle -1|\mathcal{H}_{ex}|+1\rangle & \langle -1|\mathcal{H}_{ex}| -1\rangle \end{pmatrix} = \begin{pmatrix} \Delta_0 & \Delta_1 \\ \Delta_1 & \Delta_0 \end{pmatrix} \quad (2.7)$$

with $\Delta_0 = \frac{3}{4}(a_z + \frac{9}{4}b_z)$ and $\Delta_1 = -\frac{3}{8}(b_x - b_y)$.

In the ideal case in which the QD is perfectly symmetric along the z-axis, $b_x = b_y$, Δ_1 vanishes and $|+1\rangle$ and $| -1\rangle$ are degenerate eigenstates. If that is not the case, the angular momentum M along the z-direction is not preserved and $|+1\rangle$ and $| -1\rangle$ are no eigenstates of \mathcal{H}_{ex} . The new basis can be found by diagonalising \mathcal{H}_{ex} and is described by $\frac{1}{\sqrt{2}}(|+1\rangle + |-1\rangle)$ and $\frac{1}{\sqrt{2}}(|+1\rangle - |-1\rangle)$. In figure 2.3a

2.2. Fine structure splitting

the $|XX\rangle$ decay path with splitted $|X\rangle$ eigenstates is shown. $|XX\rangle$ exhibit no splitting as the angular momentum of the electrons and holes add to zero and therefore no exchange interaction occurs. In figure 2.3b photo-luminescence spectra recorded with a linear polariser are shown.



(a) XX decay cascade without X degeneracy because of fine structure

splitting. [18]

(b) Photoluminescence spectra of X emission of a GaAs QD plotted

for different polarizer angles. In the image the effect of the linear polarization of the fine structure components is visible. [19]

Figure 2.3.: Fine structure splitting in a GaAs quantum dot.

2.3. Zero-phonon line and phonon sideband

The excitonic emission of GaAs QDs (and of solid-state quantum emitters in general) exhibits non-Lorentzian asymmetric broadening. These side bands can be traced back to a coupling to acoustic phonons [24][25]. The discussion of phonon side bands (PSBs) is based on the works of Friedrich and Haarer [26] and Peter et al. [24].

Figure 2.4 displays a schematic representation of the zero phonon line (ZPL) and PSB absorption spectrum. The intensity distribution between the two components depends strongly on temperature and can be described by the Franc-Condon principles (FCP) [27].

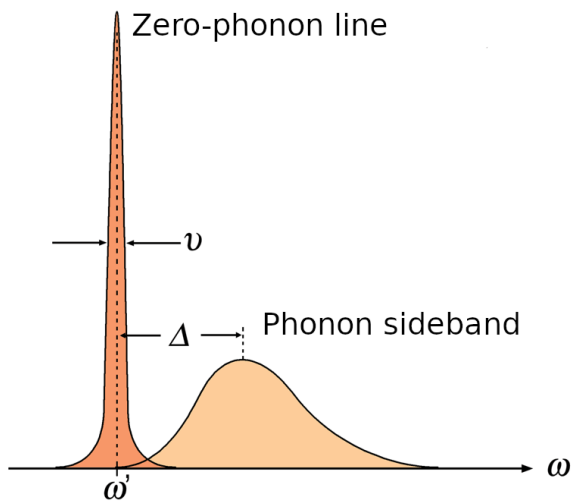
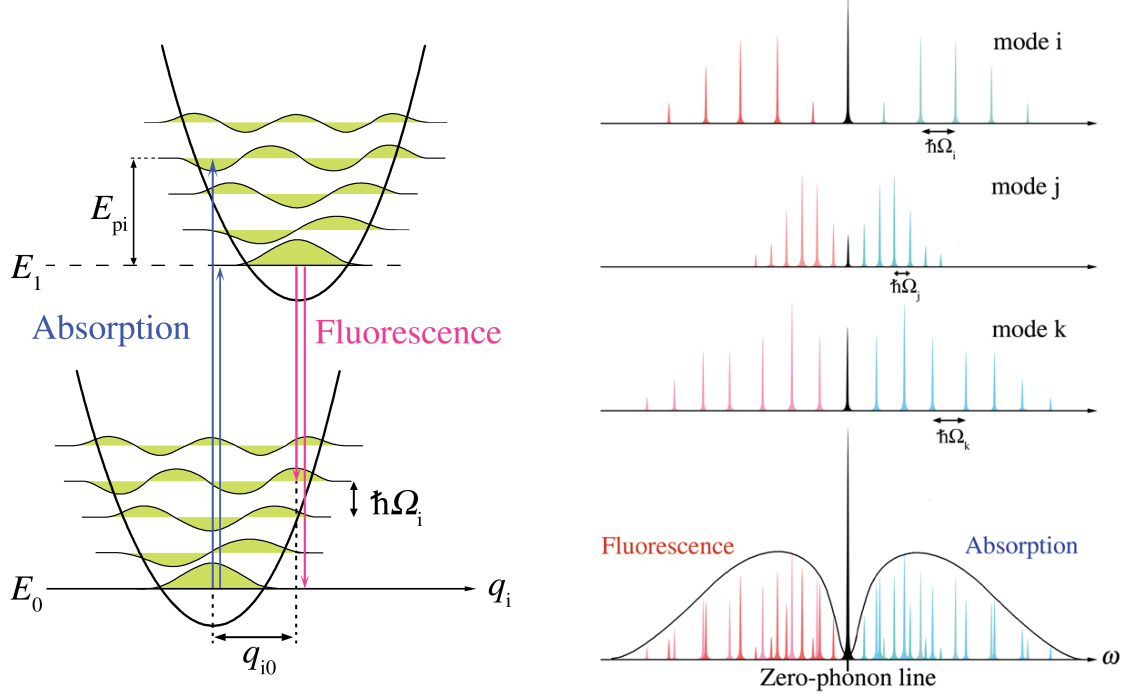


Figure 2.4.: Absorption line shape of an electronic excitation. The emission shape can be determined by mirroring the absorption shape at ω' .

The FCP state that electronic transition between ground and excited state is much faster than the motion in the lattice, which is why there is no motion along the configurational coordinates q_i during the energy transitions as depicted in figure 2.5a. The transitions can be displayed as vertical arrows with the shorter arrow describing the ZPL and the longer one describing the PSB. According to the FCP, the more the wave functions of two vibrational energy levels overlap, the likelier is the electronic transition between these two. In the case of figure 2.5a this occurs when the photon energy equals to the energy difference $E_1 - E_0$ plus three quanta of vibrational energy $E_{pi} = \hbar\Omega_i$. The emission follows the same principle.



(a) Energy spectrum of a two-level electronic system with phonon coupling. The arrows describe emission/absorption with and without phonons respectively.

(b) Three lattice normal modes (i, j, k) and the resulting emission/absorption spectrum.

Figure 2.5.: Zero-phonon line and phonon sideband. [28]

Figure 2.5a and 2.5b implicitly assume approximations in addition to the FCP. The lattice vibrational mode has to be well described by a quantum harmonic oscillator. Additionally, it is assumed that only the lowest lattice vibration is excited and that the harmonic oscillator potentials are equal in both states. These preconditions are visible in the parabolic shaped potential wells and equally spaced phonon energy levels in figure 2.5a.

Each lattice mode m leads to a different energy difference $\hbar\Omega_m$ between phonons. That is why the transitions with phonons result in a energy distribution and the zero-phonon transition add up at the electronic origin $E_1 - E_0$ as can be seen in figure 2.5b.

2. Gallium arsenide quantum dots

The theoretical limit of the spectral range of the zero-phonon line for a GaAs quantum dot can be calculated with the time-energy uncertainty relation

$$\Delta E \cdot \Delta t = \frac{h}{2\pi} \quad (2.8)$$

This gives for a typical lifetime of a GaAs quantum dot of $\Delta t = 250 \text{ ps}$

$$\Delta E = 2.64 \mu\text{eV}. \quad (2.9)$$

The frequency uncertainty can be obtained through

$$\Delta\nu = \frac{\Delta E}{h}. \quad (2.10)$$

The wavelength λ relates to ν with the Planck-Einstein relation

$$\lambda(\nu) = \frac{c}{\nu} \quad (2.11)$$

and the wavelength uncertainty $\Delta\lambda$ can be approximated with a Taylor series around ν_0

$$\Delta\lambda = -\lambda'(\nu_0) \cdot \Delta\nu. \quad (2.12)$$

With equation (2.10) and the center wavelength of the zero-phonon line λ_0 in table 2.1 this gives

$$\Delta\lambda = \frac{c}{\nu_0^2} \cdot \Delta\nu = \frac{\lambda_0^2}{c} \cdot \Delta\nu \quad (2.13)$$

$$\approx 1.0 \text{ pm} \quad (2.14)$$

In practise, the ZPL is broadened by pure-dephasing due to interaction with phonons. Together with data from Schöll et al. [29] and empirical values measured by our group, this leads to the parameters listed in table 2.1.

Table 2.1.: Parameters of GaAs quantum dots used in the laboratory of semiconductor physics department in Linz. Zero-phonon line calculates from the theoretical limit according to the lifetime of the excitonic state (as can be seen in equation (2.14)). The phonon sideband resembles data taken from Schöll et al. [29].

Quantum dot emission	Center wavelength λ_0	Spectral range $\Delta\lambda$	Waveform
Zero-phonon line	(700 to 800) nm	(1.0 to 1.4) pm	Cauchy
Phonon sideband	~0.25 nm higher than zero-phonon line	500 pm	Gauss

2.4. Optical excitation of a quantum dot

In this section, different ways of optically exciting QDs are discussed. It is based on the PhD thesis of Huber [18] and the master's thesis of Schimpf [19]. The excited states of a QD can be populated in various ways. A common way is above-band excitation, depicted in figure 2.6a. Electrons are optically excited by a laser with energies above the band gap of the QDs host material Al_{0.4}Ga_{0.6}As with $E_L = 1.92$ eV at room temperature. Subsequently, electrons and holes are captured by the QDs and relax via phonon-scattering to the lowest energy level, the s-shell. However, because of pronounced recapture processes [30] and spin scattering processes [31], above-band excitation is not favourable for entangled photon generation. Additionally, indistinguishability of the emitted photons is reduced because of fluctuating electric fields and time-jitter induced by the relaxation process. Resonant excitation of electron-hole pairs provides an alternative to alleviate these effects. As shown in figure 2.6b this technique creates electron-hole-pairs directly in the s-shell.

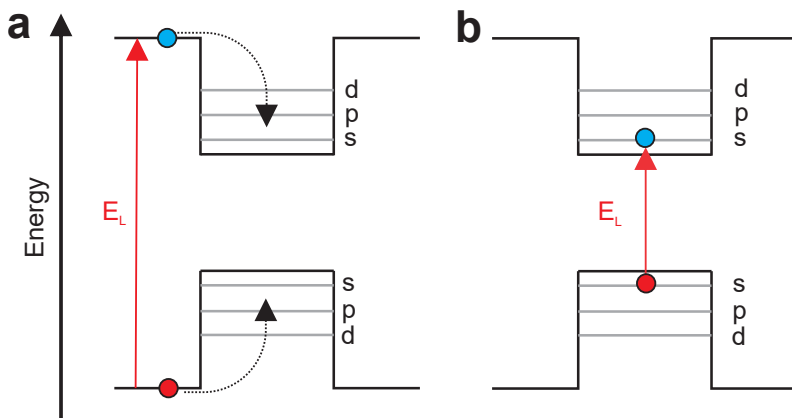


Figure 2.6.: Optical pumping of a QD by (a) above-band excitation and (b) resonant excitation [18]

Resonant excitation can be used in order to populate the $|XX\rangle$ state with near unity population probability [32]. Due to dipole-selection rules, this requires a two-photon-absorption process. Hereby, the energy of a femtosecond-pulse laser E_p is tuned to exactly the half of the XX energy with respect to the ground energy, as sketched in figure 2.7a. Because of Coulomb interaction, two times the X energy with respect to the ground energy $2 \cdot E_X$ is not equal to E_{XX} but differs by the binding energy E_B . The laser is therefore tuned to

$$E_p = E_X - E_B / 2 \quad (2.15)$$

with $E_B \approx 3.78$ meV for GaAs QDs. Resonant two-photon absorption is a third-order non-linear effect which involves two photons and electrons at once. It depends on the third-order-susceptibility $\chi^{(3)}$ of

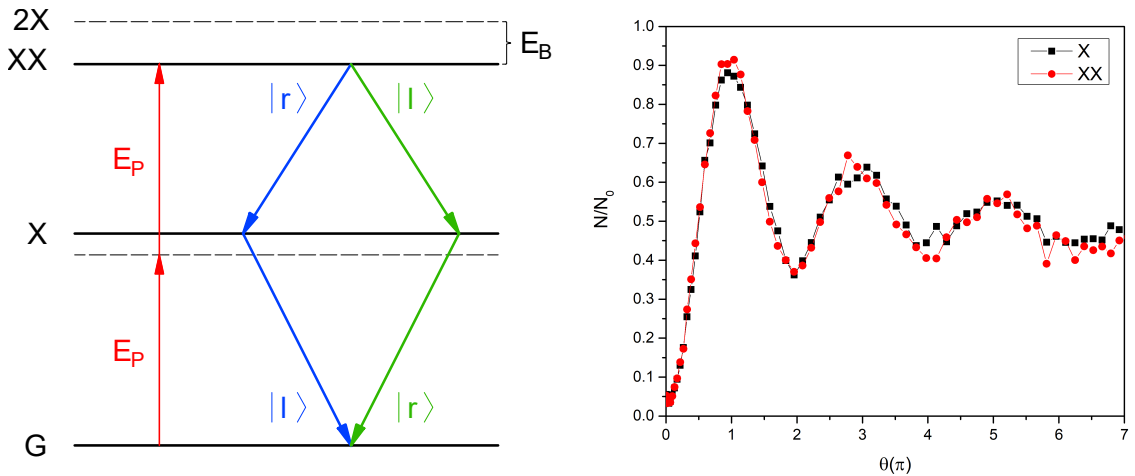
2. Gallium arsenide quantum dots

GaAs and therefore requires relatively high laser power.

As this two-level system is driven in resonance, its population exhibits Rabi oscillations. The final population of the XX can be described by

$$N_{XX} = \sin^2\left(\frac{\theta}{2}\right) \quad (2.16)$$

with θ as the pulse area in relation to the Rabi oscillations. It has to be noted that θ is not the area of the excitation pulse, but depends on it in a non-trivial way [33]. Measured Rabi oscillations of X and XX are shown in figure 2.7b [32]. Theoretically, the curve should oscillate between occupancies N/N_0 , with N_0 as the maximum population, of 0 and 1. However, as a consequence of phonon damping the occupancy converges to a purely probabilistic value of 0.5 [34].



(a) Resonant two photon excitation of XX.

The laser is tuned to $E_P = E_{XX}/2$.

(b) Rabi oscillations of X and XX as a function of the pulse area θ .

N/N_0 is the occupancy and N_0 the maximum population.

Figure 2.7.: Resonant two photon excitation [19]

2.5. Single photon emission

The XX-X decay cascade shown in figure 2.7a results in a single photon pair per emission cycle. Single photons are necessary for quantum cryptography and quantum optics in general, which motivates the following discussion of this topic based on the thesis of Huber [18]. The single photon purity of the $|XX\rangle$ to $|X\rangle$ and the $|X\rangle$ to $|G\rangle$ decay emissions, respectively, can be determined by performing a Hanbury-Brown-Twiss (HBT) experiment. An example of an HBT setup is shown in figure 2.8a and

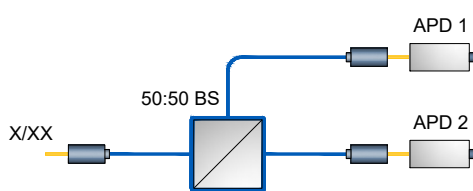
consists of two avalanche photodiodes (APDs) used as single photon detectors and a beam splitter. The measurements at the two detectors can be used in order to calculate the second-order correlation function

$$g^{(2)}(\tau) = \frac{\langle n_1(t)n_2(t+\tau) \rangle}{\langle n_1(t) \rangle \langle n_2(t+\tau) \rangle} \quad (2.17)$$

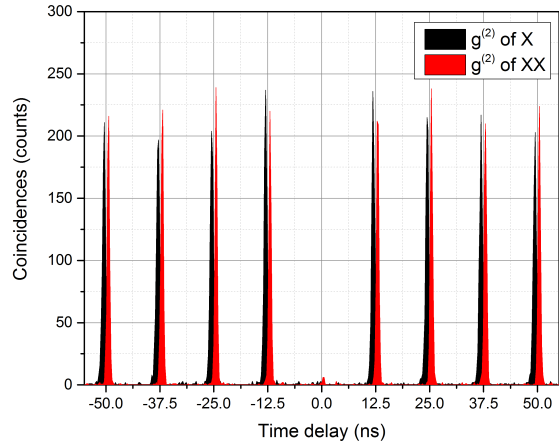
where $n_i(t)$ is the number of counts registered on APD i at time t and τ is the time delay. When a single photon enters the input of the beam splitter (BS), it can only be measured at one output, but never at both simultaneously. Assuming a perfect single photon emitter, a coincidence measurement between APD 1 and APD 2 will result in $g^{(2)}(\tau = 0) = 0$. Subsequently, side peaks are expected at $\tau_s = z/R$ with R as the repetition rate of the laser and $z \in \mathbb{Z} \setminus \{0\}$. The single photon purity can then be defined as

$$\kappa(b) = \frac{A_0(b)}{A_s(b)} \quad (2.18)$$

with A_0 as the area under $g^{(2)}(\tau)$ around $\tau = 0$ and A_s as the average area under the side peaks at τ_s . The time bin b has to be chosen so that it includes a full side peak. If b would be chosen too small it would falsely increase κ , if chosen too high it would include unnecessary much noise.



(a) Setup to measure the Hanbury-Brown-Twiss effect. Single photons can be measured only at one APDs, but not at both at the same time.



(b) Second-order auto-correlation function $g^{(2)}$ of X and XX. The low height of the peak at zero time delay compared to the height of the side peaks suggest the suitability of the quantum dot as a single photon emitter.

Figure 2.8.: Hanbury-Brown-Twiss HBT experiment [19]

3. Methods

3.1. Optical setup

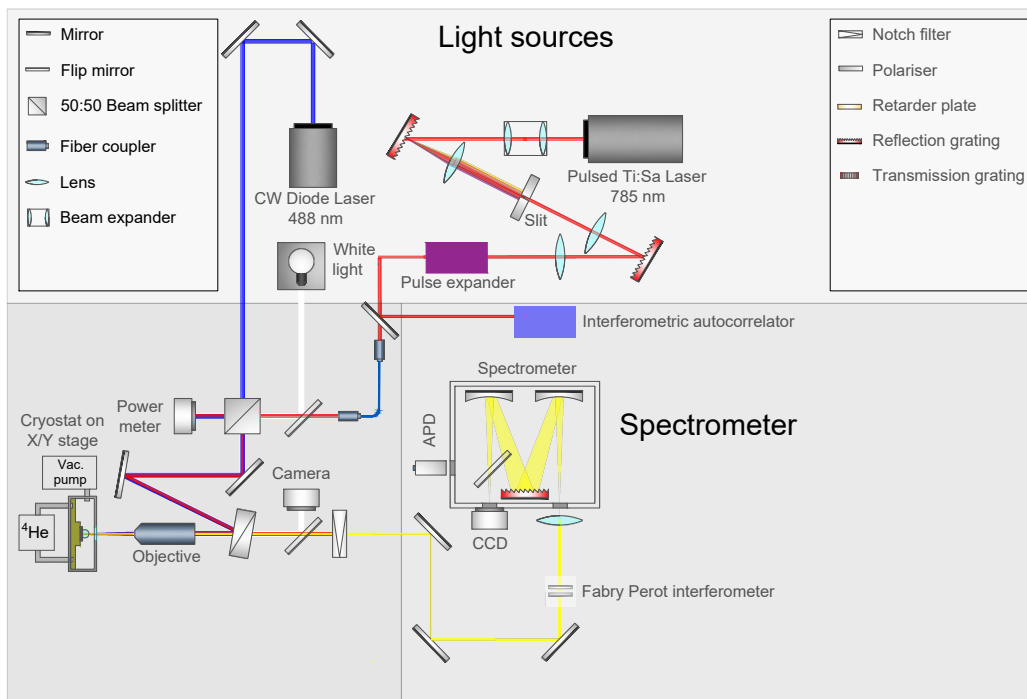


Figure 3.1.: Complete experimental setup, which was used in order to quantify the chirp of the Ti:Sa Laser and resolve spectral emission of a quantum dot [19].

The setup used for the measurements described in following chapters is sketched in figure 3.1. This setup involves a Ti:Sa laser producing pulses which are sent through a pulse shaper. Its chirp can be

3. Methods

modified with the pulse expander and measured with the interferometric autocorrelator as will be discussed in chapter 4. The CW diode laser is used in order to find a suitable QD via photoluminescence spectroscopy and the white light enhances the brightness of some QDs by reducing blinking [35]. The spectrometer is then used to measure QD emission either with a CCD or an APD.

3.2. Pulse shaper

In order to resonantly excite the $|XX\rangle$ state a pulsed Ti:Sa laser with a full width at half maximum (FWHM) pulse duration of $\tau_p \approx 100$ fs is used. Under the assumption that the laser pulse is of Gaussian shape and that it is chirp-free (more on that in chapter 4), the spectral bandwidth $\Delta\nu$ can be described by [36]

$$\Delta\nu\tau_p \approx 0.44. \quad (3.1)$$

This corresponds to a spectral range of $\Delta E = h\Delta\nu = 18.2$ meV. As can be seen in equation (2.15), the spectral range should be smaller than $E_B/2 \approx 1.89$ meV, which is not fulfilled with the laser beam alone.

The pulse shaper sketched in the upper part of figure 3.1 is used in order to tune ΔE and additionally the centre emission energy to our requirements. The laser beam is sent through a Keplerian telescope in order to expand its beam diameter from 3.4 mm to 6 mm. The beam gets dispersed by a diffraction grating and then focused by a lens so that the spectral components are ordered along the Fourier plane where a slit is placed. The centre energy can be adjusted with the slit position and the spectral range with the slit width. The setup is mirrored with an additional lens and diffraction grating, which transform the laser beam back into real space.

3.3. Micro photo-luminescence

The following chapters will investigate the optical properties of QDs. In order to achieve that, it is necessary to excite and collect light of only a single QD. This is achieved by micro photo-luminescence (MPL), which involves (i) reducing the diameter of the excitation laser beam and (ii) using samples with a low QD density [37]. (i) can be improved by using an objective, where its minimal achievable spot size d is described by the Abbe limit

$$d = \frac{\lambda}{2 \cdot NA} \quad (3.2)$$

with NA as the numerical aperture. As the wavelength of the laser λ is adjusted according to the optical properties of the QD, NA is the adjustable factor. In our laboratory, objectives between $NA = 0.42$ and $NA = 0.85$ are used, allowing laser spot sizes in the order of the excitation wavelength. A QD density of approximately $1/\lambda^2$ is therefore necessary in order to examine the emission of a single QD.

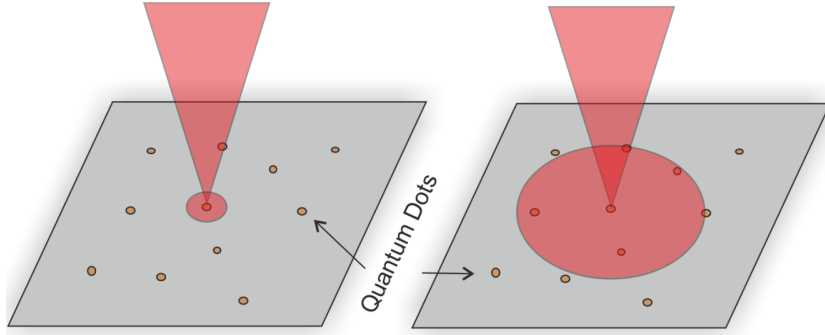


Figure 3.2.: Laser beam of different spot sizes illuminating quantum dots [37].

The sample containing the QDs is mounted inside a cryostat, which is cooled down to 4 K. This is necessary to limit spectral broadening due to phonons. The laser beam is focused on the sample by the objective and the QD emission is then collected by the very same objective and passed through a beam splitter.

4. Entangled photon generation using adiabatic rapid passage with frequency-chirped pulses

4.1. Introduction and motivation

In order to efficiently use the biexciton decay cascade, the biexciton state has to be prepared beforehand in a robust way. This chapter deals with the efficient inversion of the QD from the ground state to the biexciton level via adiabatic rapid passage (ARP). ARP uses chirped pulses, which need to be measured and deterministically adjusted in order to effectively use them. Therefore, the majority of this chapter will focus on the chirp and how to determine and adjust it, with the help of simulations and later with measurements.

4.2. Chirp

A chirped signal is a signal whose frequency changes over time. For example, the frequency of a linearly chirped signal $f(t)$ would be described by

$$f(t) = ct + f_0 \quad (4.1)$$

where f_0 is the starting frequency at $t = 0$ and c is the chirpiness. A linearly chirped sinusoidal wave is depicted in figure 4.1.

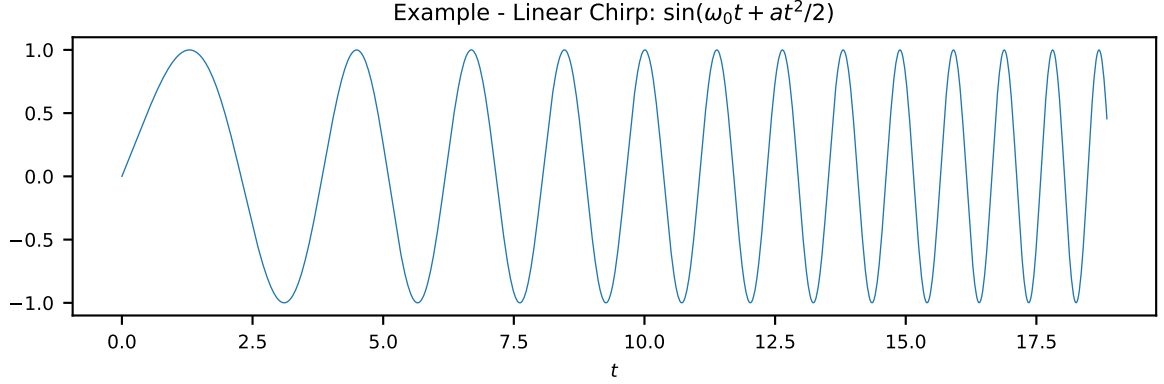


Figure 4.1.: A chirped sinusoidal wave which increases in frequency over time.

As this chapter is concentrated on exciting QDs with frequency-chirped pulses, the mathematical description of chirped laser pulses will now be discussed. The shape of the electric field of a laser $E(t)$ can be approximated by

$$E(t) \sim \text{Re} \left(f^{1/2}(t) \cdot \exp(-i\omega t - i\phi(t)) \right) \quad (4.2)$$

with the central frequency ω and the linear chirp $\phi(t)$.

Depending on the laser either a Gaussian or a hyperbolic secant describes the pulse shape more accurately [38, 39]

- Gaussian pulse:

- Pulse shape of

$$f_{gauss}(t) = \left(\frac{A_{gauss}}{\sqrt{2 \cdot \pi \cdot \tau_0 \cdot \tau}} \exp\left(-\frac{t^2}{2 \cdot \tau^2}\right) \right)^2 \quad (4.3)$$

with the normalization constant A_{gauss} , the pulse duration τ_0 , the central frequency ω and the chirp coefficient α .

- Linear chirp of

$$\phi_{gauss}(t) = \frac{\alpha_{gauss} t^2}{2} \quad (4.4)$$

where

$$\tau = \sqrt{\alpha^2 / \tau_0^2 + \tau_0^2} \quad (4.5)$$

characterizes the chirped pulse length and

$$\alpha = \alpha / (\alpha^2 + \tau_0^4) \quad (4.6)$$

is the frequency chirp rate.

- Secant pulse:

- Pulse shape of

$$f_{secant}(t) = A_{secant} \cdot \operatorname{sech}^2\left(\frac{t}{\tau_0}\right) = A_{secant} \cdot \left(\frac{2}{\exp\left(\frac{t}{\tau_0}\right) + \exp\left(-\frac{t}{\tau_0}\right)}\right)^2 \quad (4.7)$$

with the normalization constant A_{secant} , the pulse duration τ_0 , the central frequency ω and the chirp coefficient α .

- Linear chirp of

$$\phi_{secant}(t) = \alpha_{secant} \left(\frac{t}{\tau_0}\right)^2 \quad (4.8)$$

The following discussion will assume a Gaussian laser shape as described by equation (4.3) and (4.4). A simulation for E is plotted in figure 4.2 for different chirp parameters α suitable to display examples for strong and weak chirps. As can be seen there, the chirp parameter strongly influences the shape of the electric field. If E could be measured directly, the chirp could be easily estimated. This is not feasible in our case, as our Ti:Sa laser can produce laser pulses as short as 100 fs and response times of photodiodes and oscilloscopes are in the best case in the order of 200 fs. This means they cannot even measure the duration of these ultrashort pulses let alone resolve the pulse shape.

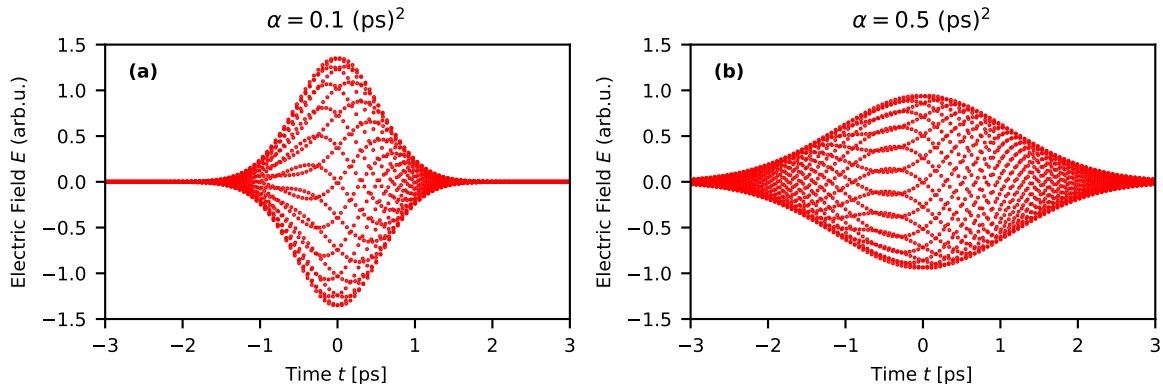


Figure 4.2.: Electric field E of Gaussian laser pulse of pulse duration $\tau_0 = 0.5$ ps for chirp of (a) $\alpha = 0.1 \text{ ps}^2$ and (b) $\alpha = 0.5 \text{ ps}^2$

4.3. Measuring the chirp with interferometric autocorrelation

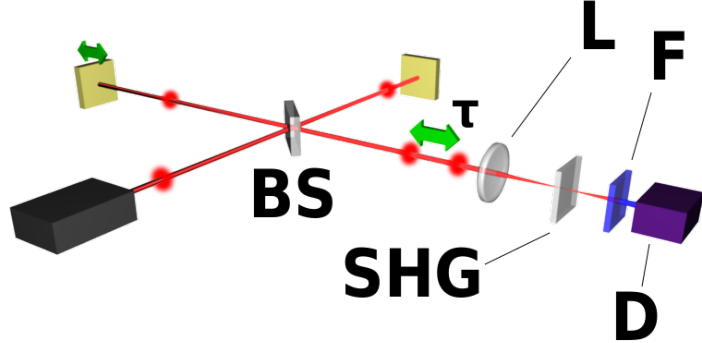


Figure 4.3.: Schematics of an interferometric autocorrelator, where **L** is a converging lens, **SHG** a second-harmonic generation crystal, **BS** a beam splitter, τ the interval between two pulses, **D** the detector and **F** a spectral filter to block the fundamental wavelength [40].

In order to estimate the pulse width τ_0 , interferometric autocorrelation (IAC) is used. Basically, a nonlinear crystal is added to a Michelson interferometer in order to generate a signal governed by

$$I_M(\tau) = \int_{-\infty}^{+\infty} \langle |(E(t) + E(t - \tau))^2|^2 \rangle dt. \quad (4.9)$$

and plotted in figure 4.4 [41]. Here, $\langle \rangle$ denotes averaging over fast oscillations of the electric field.

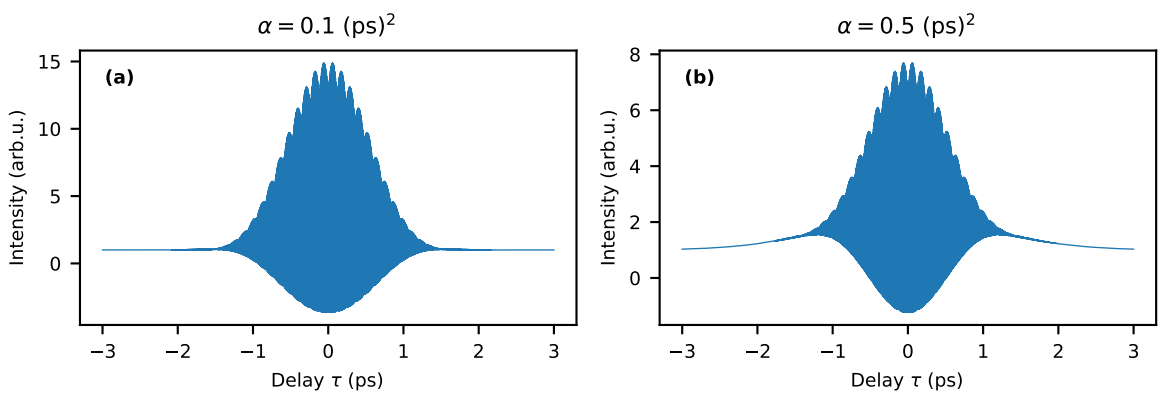


Figure 4.4.: Intensity of IAC of a Gaussian laser pulse of pulse duration $\tau_0 = 0.5$ ps without applied MOSAIC filter for chirp of (a) $\alpha = 0.1 \text{ ps}^2$ and (b) $\alpha = 0.5 \text{ ps}^2$

Under the use of equation 4.2, equation (4.9) can be expanded to

$$I(\tau) = 1 + 2 \int f(t)f(t+\tau)dt + \int f(t)f(t+\tau) \cos(2\omega\tau + 2\Delta\phi)dt \\ + 2 \int f^{1/2}(t)f^{3/2}(t+\tau) \cos(\omega\tau + \Delta\phi)dt + 2 \int f^{3/2}(t)f^{2/2}(t+\tau) \cos(\omega\tau + \Delta\phi)dt \quad (4.10)$$

where $\Delta\phi(t, \tau) = \phi(t + \tau) - \phi(t)$ and $\int f(t)dt = 1$.

As can be seen in figure 4.4, the chirp parameter α has hardly any measurable influence on the resulting signal. However, certain modifications to the IAC signal introduced by Hirayama and Sheik-Bahae [39] make it much more sensitive to the temporal chirp. It is called modified-spectrum autointerferometric correlation (MOSAIC) and performs the following transformations on the IAC spectrum: The ω terms are eliminated and the 2ω term is doubled. The MOSAIC signal is then described by

$$I_M(\tau) = 1 + 2 \int f(t)f(t+\tau)dt + 2 \int f(t)f(t+\tau) \cos(2\omega\tau + 2\Delta\phi)dt. \quad (4.11)$$

When the MOSAIC filter is applied to the data in figure 4.4, this results in a signal as shown in figure 4.5. Here the influence of the chirp is clearly visible in the lower envelope.

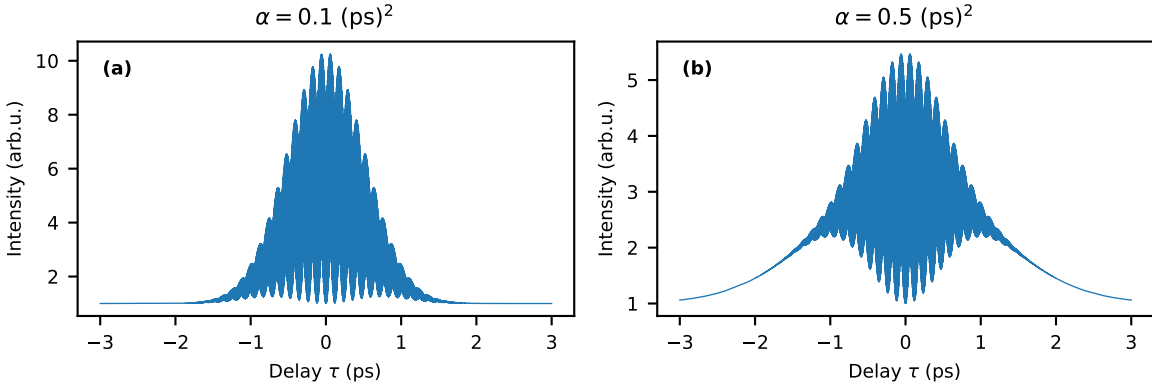


Figure 4.5.: Intensity of IAC of a Gaussian laser pulse of pulse duration $\tau_0 = 0.5$ ps for chirp of (a) $\alpha = 0.1 \text{ ps}^2$ and (b) $\alpha = 0.5 \text{ ps}^2$

4. Entangled photon generation using adiabatic rapid passage with frequency-chirped pulses

The points of the lower envelope can be obtained by determining the local minima of the signal as shown in figure 4.6.

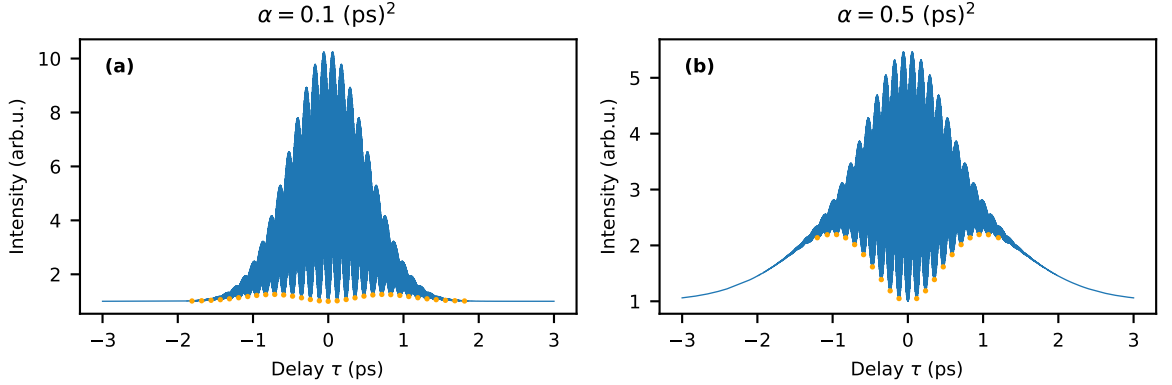


Figure 4.6.: Intensity of IAC of a Gaussian laser pulse of pulse duration $\tau_0 = 0.5$ ps with applied MOSAIC filter for chirp of (a) $\alpha = 0.1 \text{ ps}^2$ and (b) $\alpha = 0.5 \text{ ps}^2$. The orange dots are results of a numerical peak finder algorithm, executed in order to find local minima.

The lower bound (minima envelope) of the MOSAIC trace can be derived by use of a standard textbook procedure [42]

$$S_{\text{MOSAIC}}^{\min}(\tau) = 1 + 2 \cdot g(\tau) - 2 \cdot [g_s^2(\tau) + g_c^2(\tau)]^{1/2} \quad (4.12)$$

with

$$g(\tau) = \int f(t)f(t+\tau)dt \quad (4.13)$$

$$g_s(\tau) = \int f(t)f(t+\tau) \sin(2\Delta\phi)dt \quad (4.14)$$

$$g_c(\tau) = \int f(t)f(t+\tau) \cos(2\Delta\phi)dt. \quad (4.15)$$

The points of the lower envelope determined before can now be fitted in order to obtain the chirp parameter α as shown in figure 4.7. It is visible that the fitted values of α correspond to the expected values.

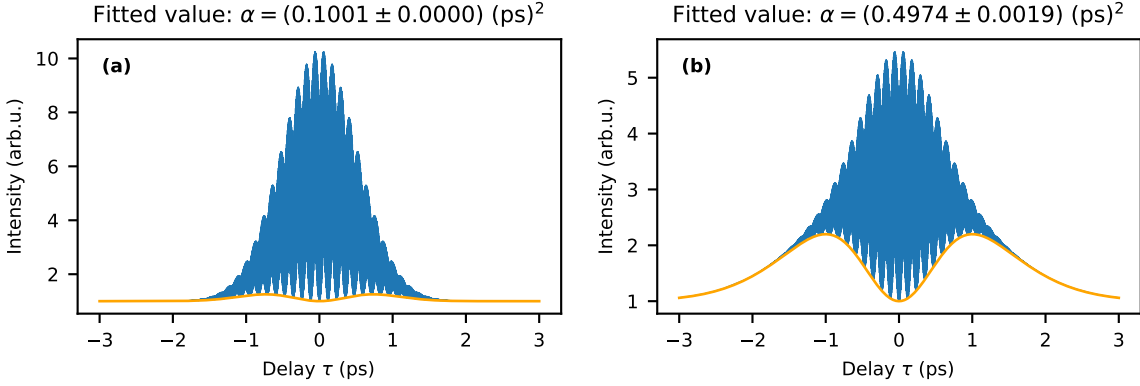


Figure 4.7.: Intensity of IAC of a Gaussian laser pulse of pulse duration $\tau_0 = 0.5$ ps with applied MOSAIC filter for chirp of (a) $\alpha = 0.1 \text{ ps}^2$ and (b) $\alpha = 0.5 \text{ ps}^2$. The orange line is a fit for the lower envelope of the MOSAIC signal in order to obtain α .

4.4. Deterministically adjusting the chirp with a pulse expander

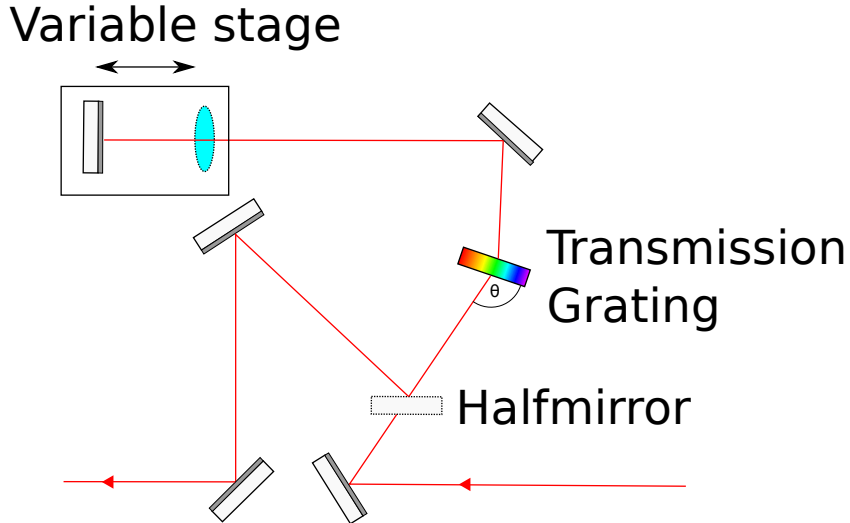


Figure 4.8.: Scheme of a folded pulse expander as described by Martinez [43]. The light enters on the right side, passes the halfmirror, and enters the system of transmission grating, lens and mirrors. Afterwards it hits the halfmirror and exits on the left hand. It induces an accumulated group velocity dispersion on the signal depending on the optical distance between the transmission grating and the lens.

In the optimal case the chirp of the pulse can be deterministically adjusted in order to most efficiently excite the QD via adiabatic rapid passage (going to be introduced in section 4.5). Grating compressors

as discussed by Martinez [43] were originally used to compensate the broadening effect fibers have on pulses. However, together with a telescope they have the inverse effect and can be used to induce a chirp. A setup like this is sketched in figure 4.8 and it will in future references in this work be called *pulse expander*. Its main elements are a transmission grating and a lens. This folded setup uses a mirror after the lens so that only one lens and one mirror are needed. The accumulated group velocity dispersion $\frac{d^2\Phi}{d\omega^2}$ can be adjusted by varying the optical distance d between the focal plane of the lens and the transmission grating and is described by

$$\frac{d^2\Phi}{d\omega^2} = k\beta^2 2d \quad (4.16)$$

where k is the wavenumber and β is given by

$$\beta = \frac{\lambda}{2\pi w_0 \cos \theta} \quad (4.17)$$

with λ denoting the centre wavelength, w_0 the beam waist (beam size at the point of its focus) and θ the emerging angle as sketched in figure 4.8.

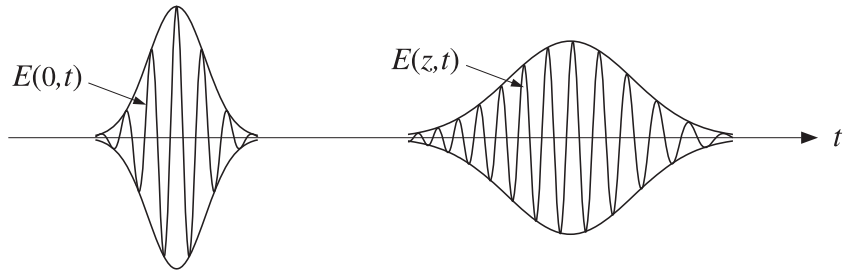


Figure 4.9.: Influence of group velocity dispersion for example inside a fiber on a Gaussian pulse [44]

As can be seen in figure 4.9, a group velocity dispersion has a similar effect on a Gaussian pulse as a chirp. In fact, the frequency chirp rate a_{gauss} introduced in equation (4.4) can be put into relation with it by: [44]

$$a_{gauss} = \frac{\frac{d^2\Phi}{d\omega^2}}{\tau_0^4 + \left(\frac{d^2\Phi}{d\omega^2}\right)^2} \quad (4.18)$$

4.5. Adiabatic rapid passage

One way to invert the QD from the ground state $|G\rangle$ to the biexciton state $|XX\rangle$ is by exciting it with a narrow-band laser pulse of constant centre frequency, which equals to half of the ground state

biexciton transition frequency. As described in equation (2.16), if the pulse area $\theta = \pi$, a population inversion from the $|G\rangle$ state to the $|XX\rangle$ occurs. However, the π -pulse method is not a generally robust scheme. In order to ensure the inversion, precise control of the field intensity is required [38]. Adiabatic rapid passage (ARP) with frequency chirped pulses is a much more robust alternative to this Rabi-flopping scheme. Here, the frequency of the laser signal is swept through resonance, starting slightly above or below the resonance frequency. The biexciton state can be populated with nearly perfect efficiency [38] if the process is performed adiabatically, i.e. if [45]

$$\Omega_0^2 \gg \left| \frac{d}{dt} \omega(t) \right| \quad (4.19)$$

where Ω_0 is the peak Rabi frequency and $\omega(t)$ is the center frequency of the laser pulse.

In figure 4.10 simulations in order to determine the final biexciton occupation for different biexciton binding energies Δ by Glässl et al. [38] are presented. Here, a linearly-chirped Gaussian laser pulse as discussed in section 4.2 was assumed.

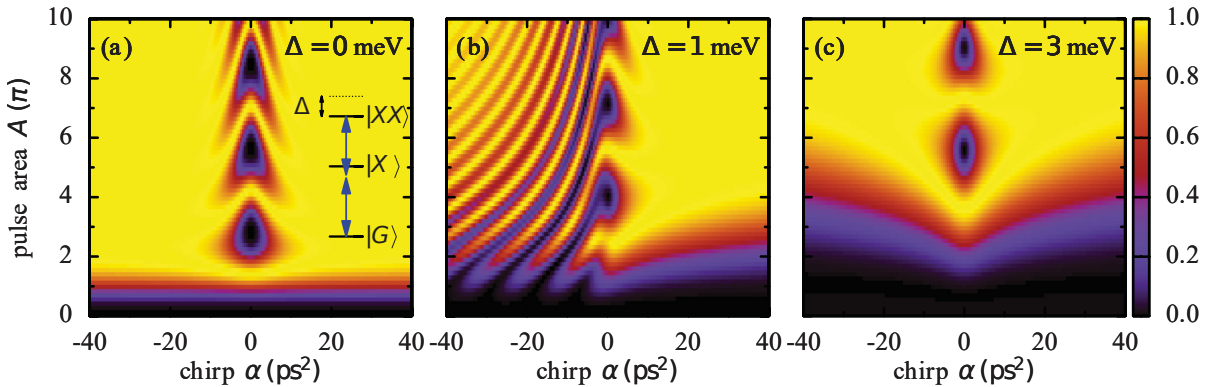


Figure 4.10.: Final biexciton occupation after chirped Gaussian pulse of pulse duration $\tau_0 = 2$ ps. It is plotted against the original pulse area A (vertical axis) and the chirp parameter α for biexciton binding energies of (a) $\Delta = 0$, (b) 1, and (c) 3 meV [38].

The central frequency is chosen so that for $\alpha = 0$ it resonates to groundstate-to-biexciton transition, which is sketched in figure 4.10. For $\alpha = 0$ Rabi oscillations are visible and their period depends strongly on the biexciton binding energy Δ . However, for $\alpha \gg 0$ biexciton preparation becomes insensitive to small variations of the pulse area A as long it exceeds a certain threshold. This is therefore the regime which would be the most suitable to work in. In the case of $\alpha < 0$ this insensitivity does not appear for moderate values of Δ as can be seen in figure 4.10(b).

4.6. Measurements and discussion

As discussed in the sections above, the final goal is to excite a QD via ARP. The first step to do that is to determine the chirp of a laser pulse which only passed the pulse shaper with the IAC. Here a laser pulse of only $\tau_0 = 344$ fs was used as the IAC can not resolve fine enough details for greater τ_0 . Even though broader peaks will be necessary in order to excite the QD with ARP, this is not a problem as the equivalent chirp can be calculated for greater τ_0 with equation (4.6).

Afterwards, a signal was measured after passing a pulse expander as discussed in section 4.4 and sketched in figure 3.1. The comparison between these two is shown in figure 4.11. Compared to the simulations in figure 4.4 it is visible that the IAC of the laser pulse without the pulse expander fits the expected shape well, while the one with the pulse expander does not. Possible reasons could be that the chirp is too high for the model used in the simulation to work or that the pulse expander introduces side effects not considered in the simulation.

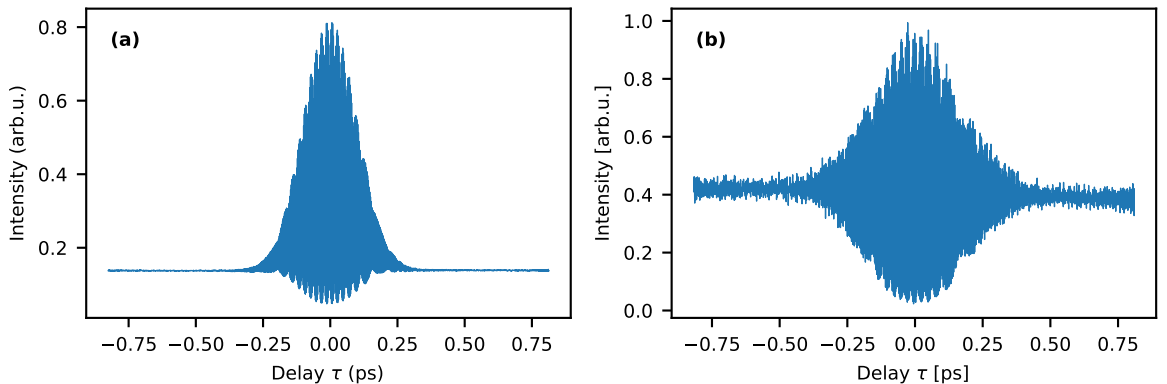


Figure 4.11.: Measured IAC of Ti:Sa Laser without (a) and with (b) pulse expander before the autocorrelator.

The same signals after applying the MOSAIC filter are shown in figure 4.12. It is visible that the lower envelopes in figure 4.12a and 4.12b do not resemble the expected ones in figure 4.5. As the laser signal without pulse expander was assumed to be relatively unchirped, it is already unexpected that the lower envelope differs that much from a constant line at zero intensity. One explanatory approach could be that the laser was already chirped to begin with. However, this would not explain why the shape of the lower envelope differs from the characteristic one of the simulation. The next approach was to send the laser without pulse shaper into the IAC. However, the envelope of the signal after

applying the MOSAIC filter showed no visible difference to the signal which has not passed a pulse shaper (depicted in figure 4.12).

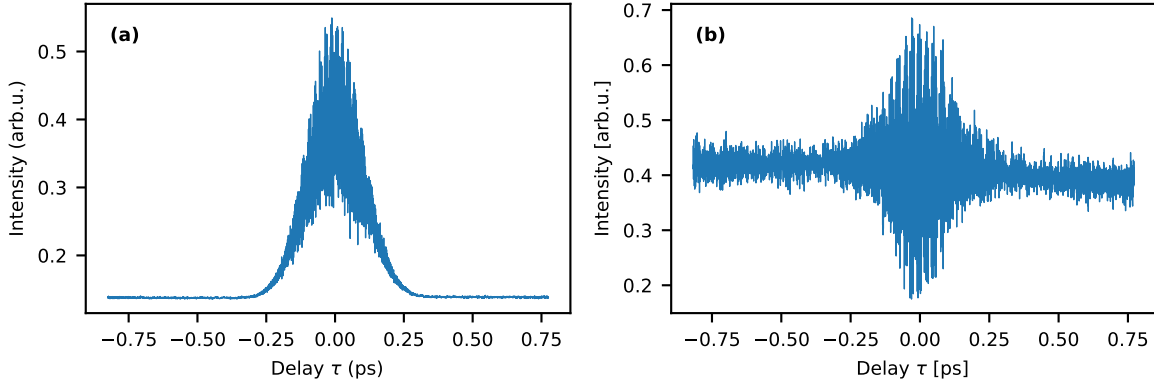


Figure 4.12.: Measured IAC of Ti:Sa Laser with applied MOSAIC filter without (a) and with (b) pulse expander before the autocorrelator.

The next step would have been to deterministically excite the QD with ARP. However, it might be advisable to repeat the same procedure with another ultrashort pulsed laser before in order to rule out that our laser is already heavily chirped to begin with. Alternatively, ARP with the pulse expander can be attempted without measuring the chirp first and iteratively adjusting the lens-grating distance until the optimum is reached.

5. Planning and building a Fabry-Pérot interferometer

5.1. Introduction and motivation

The FPI is an optical resonator developed by Charles Fabry and Alfred Pérot. An incoming light beam will only be transmitted through the resonator consisting of two semi-transparent mirrors if it fulfills the resonance condition.[46]. The resonance frequencies can be changed by adjusting the mirror distance. By measuring the intensity at the output of the FPI, this can be used to resolve fine features of an electromagnetic spectrum, like, e.g., the emitted light from the exciton-groundstate radiative decay described in section 2.3. The following chapter introduces basics of electromagnetic radiation, describes simulations performed to size the components of the FPI and displays measurement techniques used to obtain the resolved exciton spectrum.

5.2. Transverse modes of electromagnetic radiation

5.2.1. Gaussian beam

In this chapter, light beams are described by the wave picture according to Meschede [47]. They fulfil the Maxwell equations and therefore their electric field $\mathbf{E}(\mathbf{r}, t)$ fulfills the wave equation

$$\left(\nabla^2 - \frac{1}{c^2} \frac{\partial^2}{\partial t^2} \right) \mathbf{E}(\mathbf{r}, t) = 0. \quad (5.1)$$

Along the propagation direction z a light beam behaves similarly to a plane wave with constant amplitude A_0 which is a known solution to the wave equation (5.1)

$$E(z, t) = A_0 e^{-i(\omega t - kz)}. \quad (5.2)$$

5. Planning and building a Fabry-Pérot interferometer

However, far from its source light is expected to behave like a spherical wave

$$E(\mathbf{r}, t) = A_0 \frac{e^{-i(\omega t - \mathbf{k}\mathbf{r})}}{|\mathbf{k}\mathbf{r}|}. \quad (5.3)$$

To get a better understanding of the propagation of light, only paraxial (near the z-axis) parts of the spherical wave are considered. Additionally, the wave is split into its longitudinal (z-axis) part and its transversal part and beams with axial symmetry are assumed, which only depend on a transversal coordinate ρ . Under these circumstances $\mathbf{k}\mathbf{r}$ can be replaced with kr and because of $\rho \ll r, z$ the Fresnel approximation can be applied:

$$E(\mathbf{r}) = \frac{A(\mathbf{r})}{|\mathbf{k}\mathbf{r}|} e^{i\mathbf{k}\mathbf{r}} \simeq \frac{A(z, \rho)}{kz} \exp\left(i \frac{k\rho^2}{2z}\right) e^{ikz} \quad (5.4)$$

with $r = \sqrt{z^2 + \rho^2} \simeq z + \rho^2/2z$.

Equation (5.4) resembles the plane wave in equation (5.2) modulated by $\exp(ik\rho^2/2z)$. Another spherical wave solution can be obtained by applying the following replacement (z_0 is a real number)

$$z \rightarrow q(z) = z - iz_0 \quad (5.5)$$

with $q(z)$ as the complex beam parameter. Thereby, the fundamental (or TEM₀₀) Gaussian mode has been constructed

$$E(z, \rho) \simeq \frac{A_0}{kq(z)} \exp\left(i \frac{k\rho^2}{2q(z)}\right) e^{ikz}. \quad (5.6)$$

The electric and magnetic fields of Gauss modes are transversal to their propagation direction. These waveforms are called transversal electric and magnetic modes with indices (m, n) . The Gauss mode's fundamental solution is the TEM₀₀-Mode, which is the most important one and will therefore be examined in more detail in the rest of this subsection.

By executing the replacement $q(z) \rightarrow z - iz_0$ explicitly the equation (5.6) can be expressed as

$$\frac{1}{q(z)} = \frac{z + iz_0}{z^2 + z_0^2} = \frac{1}{R(z)} + i \frac{2}{kw^2(z)}, \quad (5.7)$$

with new variables z_0 , $R(z)$ and $w(z)$ being introduced. With the decomposition of the Fresnel factors into real and imaginary part, two factors can be identified: one complex phase factor, which describes the curvature of the wavefronts and a real factor, which describes the envelope of the beam. Therefore, the exponential in equation (5.6) becomes

$$\exp\left(i \frac{k\rho^2}{2q(z)}\right) \rightarrow \exp\left(i \frac{k\rho^2}{2R(z)}\right) \exp\left(-\left(\frac{\rho}{w(z)}\right)^2\right) \quad (5.8)$$

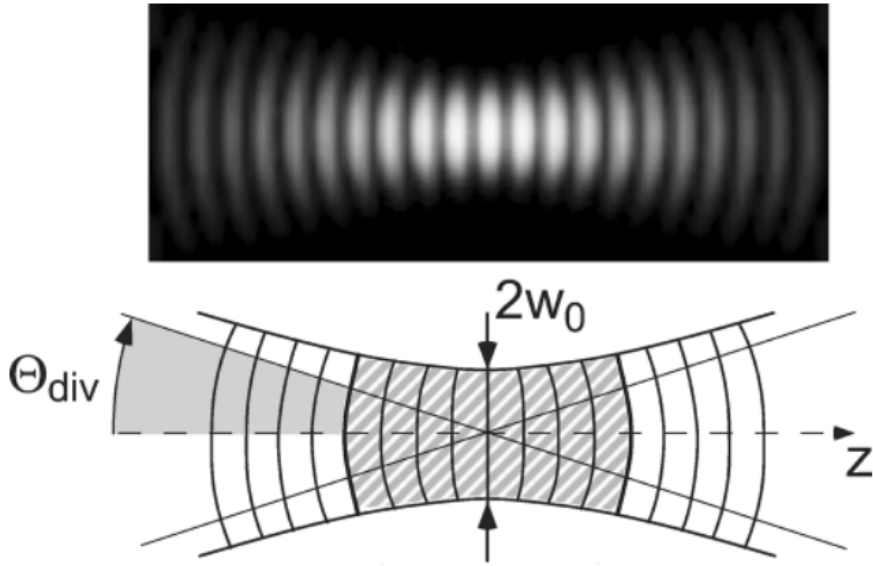


Figure 5.1.: A Gaussian beam near its beam waist. Near the center they resemble plane wave fronts, while outside they converge towards spherical wave fronts. They Rayleighzone is shaded at the lower part of the figure.[47]

For a proper description of a Gaussian beam as shown in figure 5.1 the following parameters have to be introduced

- **Evolving radius of curvature** $b(z)$:

$$b(z) = z(1 + (z_0/z)^2) \quad (5.9)$$

- **Beam waist** $2w_0$:

$$w_0^2 = \lambda z_0 / \pi \quad (5.10)$$

The beam waist $2w_0$ or beam radius w_0 describes the smallest beam cross section at $z = 0$. If the wave propagates inside a medium with the refractive index n , λ has to be replaced with λ/n . The cross section of the beam waist is then $w_0^2 = \lambda z_0 / (\pi n)$.

A Gaussian beam can be completely characterized at every point z on the beam axis either with the parameter couple (w_0, z_0) or alternatively with the real and imaginary part of $q(z)$. The parameters of the Gaussian beam are transformed by the ray transfer matrix

$$q_{out} = \frac{Aq_{in} + B}{Cq_{in} + D} \quad (5.11)$$

with the parameters A, B, C, D determined by the optical element transforming the Gaussian beam described by q_{in} . The ABCD-matrix transforms rays at distance x_1 from the optical axis at an angle θ according to

$$\begin{pmatrix} x_2 \\ \theta_2 \end{pmatrix} = \begin{pmatrix} A & B \\ C & D \end{pmatrix} \begin{pmatrix} x_1 \\ \theta_1 \end{pmatrix} \quad (5.12)$$

5.2.2. Hermite–Gaussian modes

The wave equation (5.1) can be simplified by only allowing monochromatic waves with harmonic time dependence

$$\mathbf{E}(\mathbf{r}, t) = \text{Re} \left(\mathbf{E}(\mathbf{r}) e^{-i\omega t} \right). \quad (5.13)$$

With $\omega^2 = c^2 \mathbf{k}^2$, the *Helmholtz equation* can be deduced, which only depends on the location \mathbf{r}

$$(\nabla^2 + \mathbf{k}^2) \mathbf{E}(\mathbf{r}) = 0. \quad (5.14)$$

In favor of a formal treatment of the Gaussian modes, the Helmholtz equation is split into its transversal and longitudinal contributions,

$$\nabla^2 + k^2 = \frac{\partial^2}{\partial z^2} + \nabla_T^2 + k^2 \quad \text{with} \quad \nabla_T^2 = \frac{\partial}{\partial x^2} + \frac{\partial}{\partial y^2}. \quad (5.15)$$

Additionally, the electric field \mathbf{E} of equation (5.4) is inserted into the Helmholtz equation. It is also assumed that the amplitude A only changes slowly in the order of the wavelength,

$$\frac{\partial}{\partial z} A = A' \ll kA, \quad (5.16)$$

which allows the approximation

$$\frac{\partial^2}{\partial z^2} A e^{ik\rho^2/(2z)} \frac{e^{ikz}}{kz} \simeq (2ikA' - k^2 A) e^{ik\rho^2/(2z)} \frac{e^{ikz}}{kz}, \quad (5.17)$$

and results in the *paraxial Helmholtz equation*,

$$\left(\nabla_T^2 + 2ik \frac{\partial}{\partial z} \right) A(\rho, z) = 0. \quad (5.18)$$

The fundamental solution is the TEM₀₀ mode in equation (5.6). Examples of higher modes can be found in figure 5.2.

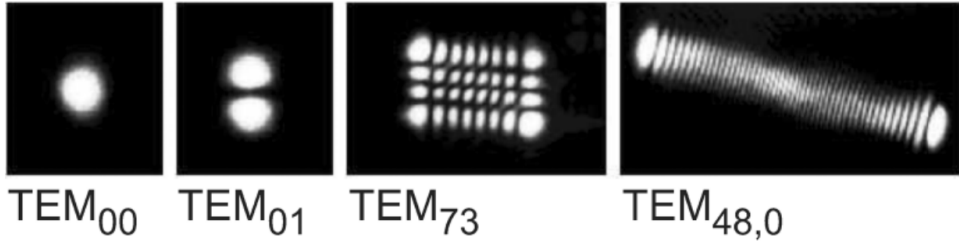


Figure 5.2.: Gaussian modes higher order of a simple Ti-sapphire laser. The asymmetry of the high modes are caused by technical inaccuracies of the resonator elements (mirrors, laser crystal).

5.3. Fundamentals of Fabry-Pérot interferometers

5.3.1. Resonator losses

For the following discussion of the FPI, a two-mirror-resonator with the reflecting surfaces facing each other and air as medium in between is assumed. The theoretical foundation is provided by the work of Ismail et al. [48].

The time the light needs for one roundtrip is given by

$$t_{RT} = \frac{2l}{c} \quad (5.19)$$

where l is the geometrical length of the resonator and c is the speed of light in air.

The photon-decay time τ_c of the interferometer is then given by

$$\frac{1}{\tau_c} = -\frac{\ln(R_1 \cdot R_2)}{t_{RT}} \quad (5.20)$$

where R_1 and R_2 are the corresponding intensity reflectivities of the mirrors.

The number of photons at frequency ν inside the resonator is described by the differential rate equation

$$\frac{d}{dt} \varphi(t) = -\frac{1}{\tau_c} \varphi(t). \quad (5.21)$$

With a number φ_s of photons at $t = 0$ the integration gives

$$\varphi(t) = \varphi_s e^{-t/\tau_c} \quad (5.22)$$

5.3.2. Resonance frequencies, free spectral range and spectral line shapes

The round-trip phase shift at frequency ν is given by

$$2\phi(\nu) = 2\pi\nu t_{RT} = 2\pi\nu \frac{2l}{c} \quad (5.23)$$

where $\phi(\nu)$ is the single-pass phase shift between the mirrors.

Resonances are visible for frequencies ν at which the light interferes constructively after one round trip. Two adjacent resonance frequencies differ in their round trip phase shift by 2π . Hence, the free spectral range $\Delta\nu_{FSR}$, the frequency difference between two adjacent resonance frequencies, can be calculated from equation (5.23)

$$2\Delta\phi_{FSR} = 2\pi \quad (5.24)$$

$$\Rightarrow 2\pi\Delta\nu_{FSR} \frac{2l}{c} = 2\pi \quad (5.25)$$

$$\Rightarrow \Delta\nu_{FSR} = \frac{c}{2l} \quad (5.26)$$

According to equation (5.22) the number of photons decays with the photon-loss time τ_c . With $E_{q,s}$ representing the initial amplitude, the electric field at ν_q is given by

$$E_q(t) = \begin{cases} E_{q,s} \cdot e^{i2\pi\nu_q t} \cdot e^{-t/(2\tau_c)} & t \geq 0 \\ 0 & t < 0 \end{cases}. \quad (5.27)$$

The Fourier transformation of the electric field can be expressed as

$$\tilde{E}_q(\nu) = \int_{-\infty}^{\infty} E_q(t) e^{-i2\pi\nu t} dt = E_{q,s} \int_0^{\infty} e^{[1/(2\tau_c) + i2\pi(\nu - \nu_q)]t} dt = E_{q,s} \frac{1}{(2\tau_c)^{-1} + i2\pi(\nu - \nu_q)}. \quad (5.28)$$

The normalized spectral line shape per unit frequency is then given by

$$\tilde{\gamma}_q(\nu) = \frac{1}{\tau_c} \left| \frac{\tilde{E}_q(\nu)}{E_{q,s}} \right|^2 = \frac{1}{\tau_c} \left| \frac{1}{(2\tau_c)^{-1} + i2\pi(\nu - \nu_q)} \right|^2 = \frac{1}{\tau_c} \frac{1}{(2\tau_c)^{-2} + 4\pi^2(\nu - \nu_q)^2} \quad (5.29)$$

$$= \frac{1}{\pi} \frac{1/(4\pi\tau_c)}{1/(4\pi\tau_c)^2 + (\nu - \nu_q)^2} \quad (5.30)$$

with $\int \tilde{\gamma}_q(\nu) d\nu = 1$.

By defining the full-width-at-half-maximum linewidth (FWHM) $\Delta\nu_c$, $\tilde{\gamma}_q(\nu)$ can be obtained

$$\Delta\nu_c = \frac{1}{2\pi\tau_c} \Rightarrow \tilde{\gamma}_q(\nu) = \frac{1}{\pi} \frac{\Delta\nu_c/2}{(\Delta\nu_c/2)^2 + (\nu - \nu_q)^2}. \quad (5.31)$$

Afterwards the Cauchy lines are normalized so that the peak is at unity

$$\gamma_{q,L}(\nu) = \frac{\pi}{2} \Delta\nu_c \tilde{\gamma}_q(\nu) = \frac{(\Delta\nu_c)^2}{(\Delta\nu_c)^2 + 4(\nu - \nu_q)^2} \quad (5.32)$$

with $\gamma_{q,L}(\nu_q) = 1$.

5.3.3. Airy distribution of Fabry-Pérot interferometers

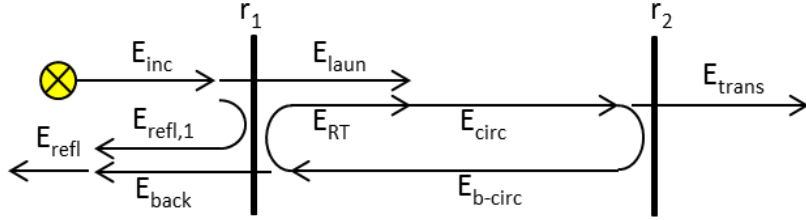


Figure 5.3.: FPI with electric field mirror reflectivities r_1 and r_2 . Indicated in this figure are the electric fields resulting from an incoming E_{inc} , the reflected field $E_{refl,1}$ and transmitted field E_{laun} . E_{circ} and $E_{circ,b}$ circulate inside the resonator, resulting in E_{RT} after one round-trip. E_{back} is the backwards transmitted field.[49]

The response of the FPI is calculated with the circulating-field approach [48], where a steady-state is assumed. E_{circ} is the result of E_{laun} interfering with E_{RT} . E_{laun} is the transmission of the incoming light E_{inc} and E_{RT} is E_{circ} after one round-trip in the resonator, i.e., after the outcoupling losses of mirror 1 and 2. Therefore, the field E_{circ} can be calculated from E_{laun} by

$$E_{circ} = E_{laun} + E_{RT} = E_{laun} + r_1 r_2 e^{-i2\phi} E_{circ} \Rightarrow \frac{E_{circ}}{E_{laun}} = \frac{1}{1 - r_1 r_2 e^{-i2\phi}} \quad (5.33)$$

where r_1 and r_2 are the electric-field reflectivities of mirror 1 and 2.

The generic Cauchy distribution only considers light inside the mirrors and is defined as

$$A_{circ} = \frac{I_{circ}}{I_{laun}} = \frac{|E_{circ}|^2}{|E_{laun}|^2} = \frac{1}{|1 - r_1 r_2 e^{-i2\phi}|^2} = \frac{1}{(1 - \sqrt{R_1 R_2})^2 + 4\sqrt{R_1 R_2} \sin^2(\phi)} \quad (5.34)$$

by using

$$\begin{aligned} |1 - r_1 r_2 e^{-i2\phi}|^2 &= |1 - r_1 r_2 \cos(2\phi) + i r_1 r_2 \sin(2\phi)|^2 = [1 - r_1 r_2 \cos(2\phi)]^2 + r_1^2 r_2^2 \sin^2(2\phi) \\ &= 1 + R_1 R_2 - 2\sqrt{R_1 R_2} \cos(2\phi) = (1 - \sqrt{R_1 R_2})^2 + 4\sqrt{R_1 R_2} \sin^2(\phi) \end{aligned}$$

and additionally $R_i = r_i^2$ and $\cos(2\phi) = 1 - 2\sin^2(\phi)$.

5. Planning and building a Fabry-Pérot interferometer

Commonly, light is sent through the FPI. Therefore the following sections will use the Airy distribution A'_{trans} described by

$$A'_{trans} = \frac{I_{trans}}{I_{inc}} = \frac{I_{circ} \cdot (1 - R_2)}{I_{laun} / (1 - R_1)} = (1 - R_1)(1 - R_2) A_{circ} = \frac{(1 - R_1)(1 - R_2)}{(1 - \sqrt{R_1 R_2})^2 + 4\sqrt{R_1 R_2} \sin^2(\phi)} \quad (5.35)$$

with $\phi = \frac{\pi v}{\Delta\nu_{FSR}}$.

A'_{trans} is displayed in figure 5.4 for $R_1 = R_2$. The peak value at one of its resonance frequencies calculates as follows

$$\max(A'_{trans}) = \frac{(1 - R_1)(1 - R_2)}{(1 - \sqrt{R_1 R_2})^2} \stackrel{R_1=R_2}{=} 1. \quad (5.36)$$

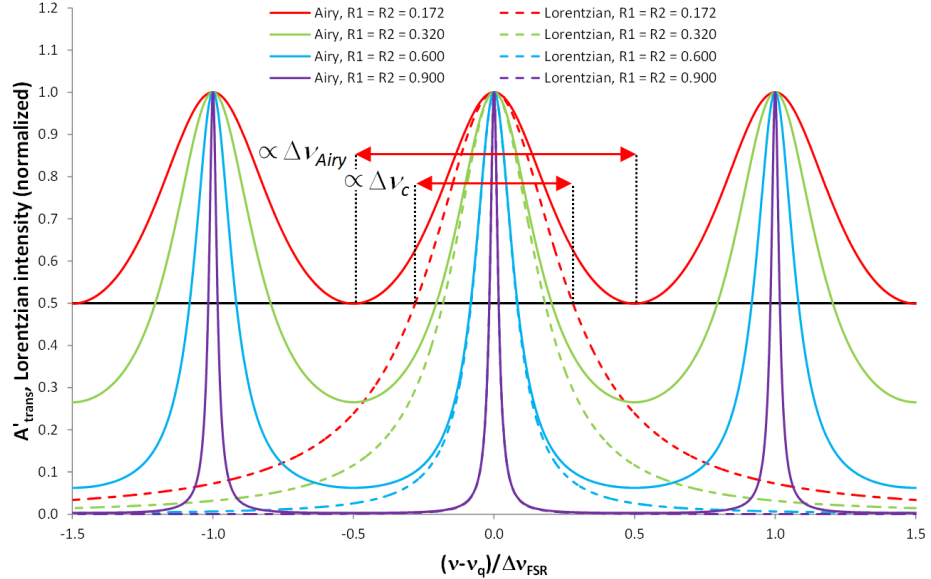


Figure 5.4.: Airy distribution A'_{trans} as described in equation (5.35) compared to the Cauchy lines $\gamma_{q,L}$ as described in equation (5.32) [49].

5.3.4. Airy linewidth and finesse

The Airy linewidth is defined as the FWHM of A'_{trans} . It can be set in relation with the free spectral range $\Delta\nu_{FSR}$ and the mirror reflectivities as follows.

A'_{trans} decreases to half of its peak value at $A'_{trans}(v_q)/2$ when the phase shift ϕ changes by the amount

$\Delta\phi$ so that the denominator of A'_{trans} in equation (5.35) is twice as big

$$\left(1 - \sqrt{R_1 R_2}\right)^2 = 4\sqrt{R_1 R_2} \sin^2(\Delta\phi) \quad (5.37)$$

$$\Rightarrow \Delta\phi = \arcsin\left(\frac{1 - \sqrt{R_1 R_2}}{2\sqrt[4]{R_1 R_2}}\right) \quad (5.38)$$

With equation (5.23) and (5.26), the phase shift can be expressed as

$$\phi = \frac{\pi\nu}{\Delta\nu_{FSR}} \quad (5.39)$$

$$\Rightarrow \Delta\phi = \frac{\pi(\Delta\nu_{Airy}/2)}{\Delta\nu_{FSR}}. \quad (5.40)$$

Therefore, with equation (5.38) and (5.40) the FWHM linewidth is given by

$$\Delta\nu_{Airy} = \Delta\nu_{FSR} \frac{2}{\pi} \arcsin\left(\frac{1 - \sqrt{R_1 R_2}}{2\sqrt[4]{R_1 R_2}}\right). \quad (5.41)$$

The finesse of the Airy distribution of a FPI is defined as

$$F_{Airy} := \frac{\Delta\nu_{FSR}}{\Delta\nu_{Airy}} = \frac{\pi}{2} \left[\arcsin\left(\frac{1 - \sqrt{R_1 R_2}}{2\sqrt[4]{R_1 R_2}}\right) \right]^{-1} \quad (5.42)$$

and is therefore only dependent on the mirror reflectivities R_1 and R_2 .

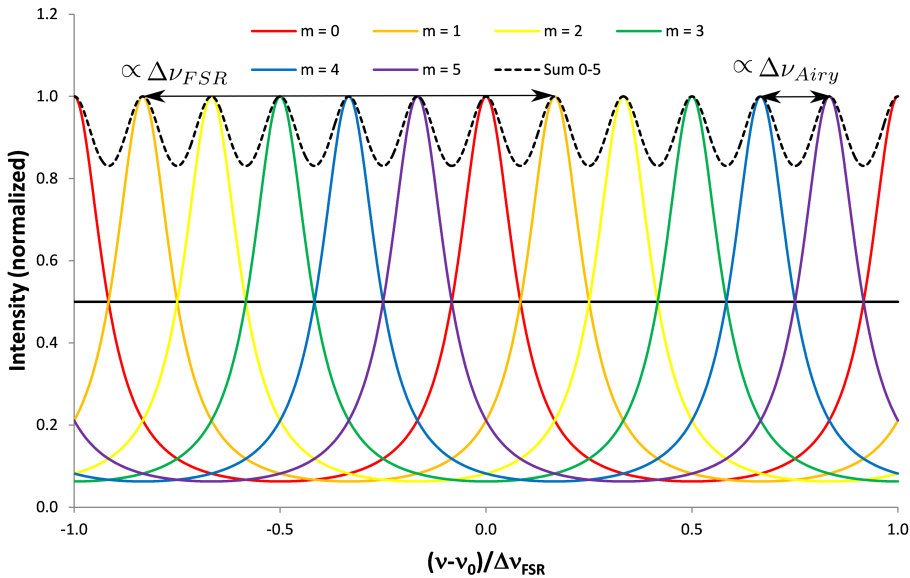


Figure 5.5.: Demonstration of the physical meaning of the Airy finesse F_{Airy} . The coloured lines are Airy distributions created by light at distinct frequencies ν_m , while scanning the resonator length. When the light occurs at frequencies $\nu_m = \nu_q + m\Delta\nu_{Airy}$, the adjacent Airy distributions are separated from each other by ν_{Airy} , therefore fulfilling the Taylor criterion. Since in this example $F_{Airy} = 6$ exactly six peaks fit inside the free spectral range. As can be seen in the figure the Airy finesse F_{Airy} quantifies the maximum number of peaks that can be resolved [49].

The Airy finesse is the determining property when it comes to the spectral resolution of the FPI. This can be made visible by comparing its meaning with the Taylor criterion for the resolution of two adjacent peaks. The Taylor criterion states that two spectral lines are resolvable when the separation of the maxima is greater than their FWHM. As displayed in figure 5.5, the Airy finesse is equal to the number of Airy distributions originating from light at certain frequencies ν_m which do not overlap at a point higher than half of their maxima. Hence, the Airy finesse describes the spectral resolution in a way that is consistent with the Taylor criterion.

5.3.5. Mode matching and spatial filtering

One fundamental challenge of Fabry Pérot interferometry is how to efficiently couple an incident beam of light into a given mode of the resonator. The following discussion is based on the work of Yariv, Yeh, and Yariv [50] and Meschede [47].

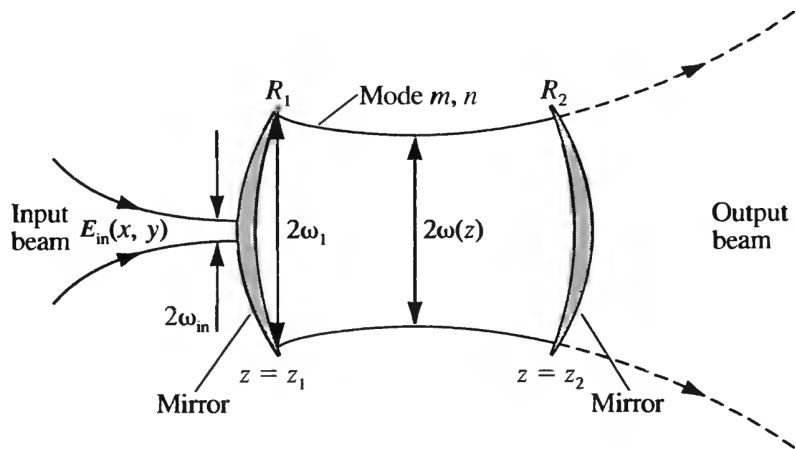


Figure 5.6.: Incident monochromatic beam of light exciting transverse mode m, n of a resonator [50]

As sketched in figure 5.6, an input beam E_{in} propagates into the resonator with curved mirrors and potentially excites its modes $E_{mn}(x, y)$, where m, n are the transverse mode integers of the Gaussian beam of the optical resonator. Since $E_{mn}(x, y)$ describes a complete orthogonal set of wavefunctions they satisfy

$$\iint E_{mn}(x, y) E_{m'n'}^*(x, y) dx dy = 0 \quad \text{unless } m = m' \text{ and } n = n'. \quad (5.43)$$

and

$$E_{in}(x, y) = \sum_{mn} a_{mn} E_{mn}(x, y) \quad (5.44)$$

where a_{mn} are constants. By multiplying both sides of equation (5.44) with E_{mn}^* , integrating over the whole x - y -plane and using equation (5.43), the following expression can be obtained

$$a_{mn} = \frac{\iint E_{in}(x, y) E_{mn}^*(x, y) dx dy}{\iint E_{mn}(x, y) E_{mn}^*(x, y) dx dy} \quad (5.45)$$

The efficiency of coupling an incident field into a spatial mode E_{mn} is defined as

$$\eta_{mn} = \frac{\text{Power coupled into mode } mn}{\text{Total incident power}} = \frac{\iint |a_{mn} E_{mn}(x, y)|^2 dx dy}{\iint |E_{in}(x, y)|^2 dx dy}. \quad (5.46)$$

By inserting equation (5.45) into equation (5.46) the following expression can be obtained

$$\eta_{mn} = \frac{|\iint E_{in}(x, y) E_{mn}^*(x, y) dx dy|^2}{\iint |E_{in}(x, y)|^2 dx dy \cdot \iint |E_{mn}(x, y)|^2 dx dy}. \quad (5.47)$$

From equation (5.47), it can be deduced that for an input beam with the *same* spatial dependency as the mode to be excited

$$E_{in}(x, y) \sim E_{mn}(x, y). \quad (5.48)$$

Under this condition, all of the incident power goes into E_{mn} , i.e. $\eta_{mn} = 1$ and all other $\eta_{m'n'}$ are zero. Usually, the fundamental TEM₀₀ mode is desired and equation (5.47) implies that a pure Gaussian beam excites only the fundamental mode and the interferometer will then irradiate a pure Gaussian beam as well. In practice, additional measures are necessary such as matching the radius of curvature by Gaussian beam focusing.

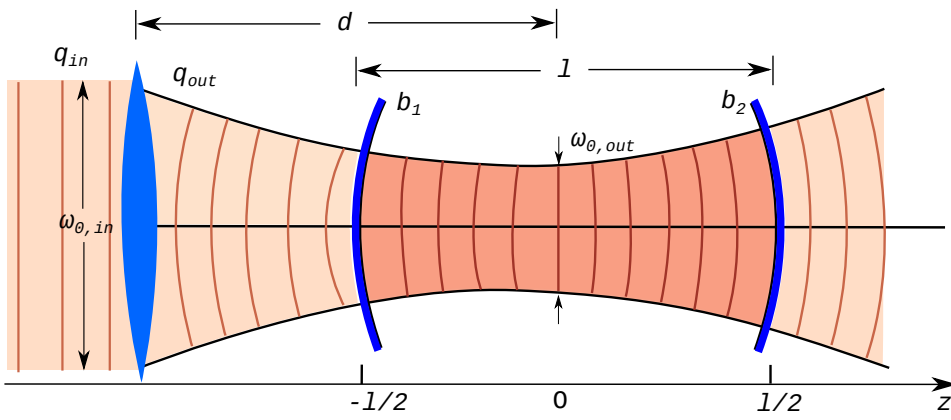


Figure 5.7.: Mode matching of an Gaussian beam into a Fabry Pérot interferometer. Incoming Gaussian beam described by q_{in} transformed by a lens into a Gaussian beam described by q_{out} . The parameters b_1 and b_2 describe the radii of the two mirrors.

5. Planning and building a Fabry-Pérot interferometer

In order to match the radius of curvature of the incoming Gaussian beam with the radius of curvature of the resonator a lens is inserted as depicted in figure 5.7. Light with a beam radius of w_{01} gets focused into the resonator. Transformations by thin lenses can be described with the ray transfer matrix introduced in subsection 5.2.1:

$$\begin{pmatrix} A & B \\ C & D \end{pmatrix} = \begin{pmatrix} 1 & 0 \\ \frac{-1}{f} & 1 \end{pmatrix} \quad (5.49)$$

with f as the wavelength of the lens. The incoming beam described by q_{in} is transformed by the lens into a beam described by q_{out} according to equation (5.10) and (5.11)

$$q_{in} = z + i \frac{\pi n w_{0,in}^2}{\lambda} \quad \text{and} \quad q_{out} = \frac{q_{in}}{q_{in} \cdot \frac{-1}{f} + 1} = z + i \frac{\pi n w_{0,out}^2}{\lambda} \quad (5.50)$$

with $n \approx 1$ for air. Together with equation (5.10) the following relation can be deduced

$$w_{0,out}^2 = \frac{w_{0,in}^2}{\left(1 - \frac{z}{f}\right)^2 + \left(\frac{\pi w_{0,in}}{\lambda f}\right)^2}. \quad (5.51)$$

The radii of curvature have to match in order to ensure that the beam returns the same way after being reflected by one mirror. For given mirrors (described by b_{mirror}) and lens (described by f) the input beam waist has to be adjusted according to equation (5.9) and (5.10)

$$b_{mirror} \stackrel{!}{=} b_{gauss}(z = l/2) \quad (5.52)$$

$$b_{mirror} \stackrel{!}{=} \frac{l}{2} \left(1 + \left(\frac{2z_{0,out}}{l}\right)^2\right) \quad (5.53)$$

$$b_{mirror} \stackrel{!}{=} \frac{l}{2} \left(1 + \left(\frac{2w_{0,out}^2 \pi}{l \lambda}\right)^2\right). \quad (5.54)$$

Inserting equation (5.54) into equation (5.51) results in the condition for mode matching

$$b_{mirror} = \frac{l}{2} \left(1 + \left(\frac{2w_{0,in}^2 \pi}{\left(\left(1 - \frac{z}{f}\right)^2 + \left(\frac{\pi w_{0,in}}{\lambda f}\right)^2\right) l \lambda}\right)^2\right). \quad (5.55)$$

One way to further suppress higher modes is *spatial filtering*. It can be seen in figure 5.2 that the effective area of a mode increases with its order (m, n). Figure 5.8 shows one way to suppress higher modes consisting of a focusing lens and a pinhole whose diameter matches the one of the TEM₀₀ mode.

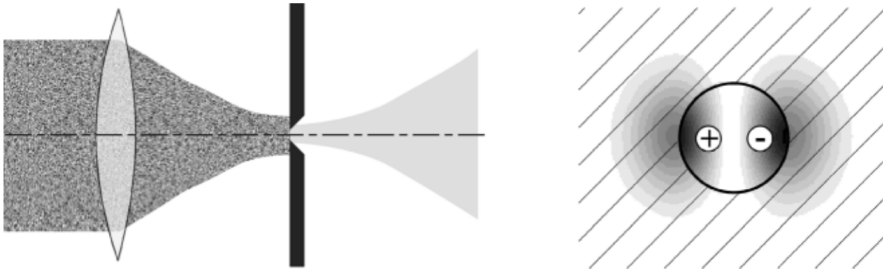


Figure 5.8.: Spatial filtering of Gauss modes. In front of the aperture, the beam consists of a superposition of multiple Gauss modes. A TEM₀₁ beam is displayed as an example of how higher modes can be suppressed by an aperture. [47]

5.3.6. Confocal setup

If the incoming beam would represent a perfect TEM₀₀ mode, spatial filtering would not be necessary and mode matching would be easy. Unfortunately, this can not always be guaranteed and counteractions like mode matching and spatial filtering discussed in subsection 5.3.5 are tedious and error prone. Arranging the mirrors of an FPI into a confocal arrangement reduces the need for these measures. By giving up the ability to choose different free spectral ranges with a given pair of mirrors, the confocal setup liberates from mode matching considerations as the cavity is mode degenerate, i.e. the frequencies of certain axial and transverse cavity modes are the same. The following discussion is based on the work of Hercher [51].

A quasi-monochromatic beam of wavelength λ_0 is composed of transverse modes TEM_{mnq}, where the subscripts m and n denote the amplitude distribution of the normal mode on a surface of constant phase and q the number of axial modes inside the resonator. Each of these modes resonates for mirror separations satisfying

$$l = \frac{\lambda_0}{2} \{q + (1 + m + n) \cos^{-1} [(1 - l/b_1)(1 - l/b_2)]^{1/2}\} \quad (5.56)$$

where the parameters b_1 and b_2 describe the radii of the two mirrors as can be seen in figure 5.7.

For the confocal setup $l = b_1 = b_2$ justifies the approximation

$$l \approx \frac{\lambda_0}{2} [q + (1 + m + n)]. \quad (5.57)$$

The modes resonate at mirror separations of either

$$l = \frac{\lambda_0}{2}(p+1) \quad p \in \mathbb{N} \text{ and } (m+n) \text{ even,} \quad (5.58)$$

$$l = \frac{\lambda_0}{2}(p) \quad p \in \mathbb{N} \text{ and } (m+n) \text{ odd.} \quad (5.59)$$

If mode matching is not performed, it can be assumed that the incoming beam consists of an approximately equal number of even and odd transverse modes. The resonance cavity length l does not depend on n, m and q anymore but only on one integer p . The transversal modes are degenerate and fulfil

$$l = \frac{\lambda_0 p}{2}. \quad (5.60)$$

It can be additionally concluded from equation (5.60) that a change of $\lambda_0/2$ in the mirror separation scans through one free spectral range.

5.4. Simulation

The goal in building up a scanning FPI is to resolve features of the emission spectra of GaAs quantum dots described in chapter 2. More precisely, it is intended to resolve the shape of the ZPL and the PSB. Equation 5.42 shows that the finesse is constant for a given pair of mirrors. If the spectrum to be resolved is broad, a higher free spectral range $\Delta\nu_{FSR}$ has to be chosen, at the expenses of resolution. If the spectrum contains fine details which need to be resolved, a lower ν_{Airy} has to be chosen, which results in a lower free spectral range $\Delta\nu_{FSR}$. Hence, the thin ZPL and the broad PSB can not be resolved with the same setup. Instead, the mirror distances have to be adjusted and in the confocal setup discussed in subsection 5.3.6 the mirrors have to be changed as well.

In absence of spectral broadening due to charge noise, the zero-phonon line is described by a Cauchy distribution

$$\Phi_{ZPL}(\lambda) = \frac{1}{\pi \cdot \Delta\lambda_{ZPL} \cdot 0.5 \left[1 + \left(\frac{\lambda - \lambda_{0,ZPL}}{\Delta\lambda_{ZPL} \cdot 0.5} \right)^2 \right]} \quad (5.61)$$

with $\lambda_{0,zero}$ as the center wavelength and $\Delta\lambda_{ZPL}$ as the spectral range of the zero-phonon line which can be found in table 2.1.

The phonon side band can be described by a Gauss distribution

$$\Phi_{PSB}(\lambda) = \frac{1}{\sqrt{2 \cdot \pi \cdot \Delta\lambda_{PSB}^2}} \cdot \exp \left(-\frac{(\lambda - \lambda_{0,PSB})^2}{2 \cdot \Delta\lambda_{PSB}^2} \right) \quad (5.62)$$

5.4. Simulation

with $\lambda_{0,PSB}$ as the center wavelength and $\Delta\lambda_{PSB}$ as the spectral range of the phonon side band which can be found in table 2.1 as well.

Together they describe the excitonic emission of the QD

$$\Phi_{dot}(\lambda) = \Phi_{ZPL}(\lambda) + \Phi_{PSB}(\lambda) \quad (5.63)$$

depicted in figure 5.9.

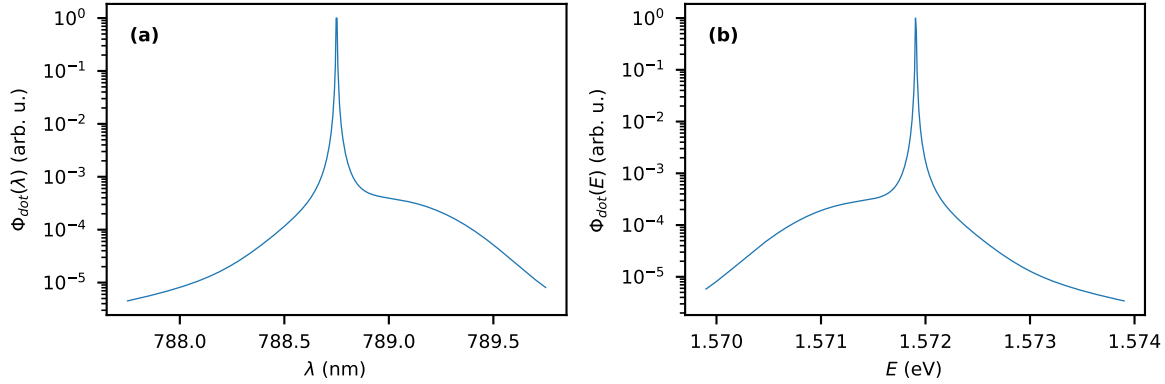


Figure 5.9.: Simulated exciton emission of a GaAs quantum dot plotted dependant on (a) the wavelength λ or (b) the energy E .

The parameters can be found in table 2.1.

$\Phi_{dot}(E)$ is transmitted through the FPI. As discussed the mirror distance l is adjusted to a value which depends on whether a resolved ZPL or a resolved PSB is desired. A comparison of the FPI transmission $A'_{trans}(E)$ described in equation 5.35 with $R_1 = R_2 = 98\%$ and $\Phi_{dot}(E)$ is shown in figure 5.10.

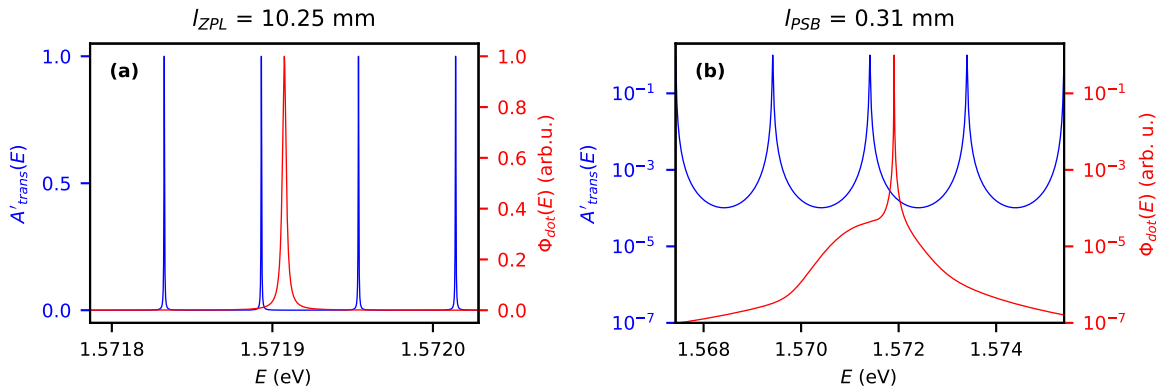


Figure 5.10.: The exciton emission $\Phi_{dot}(E)$ (red) compared to the transmission of the FPI modes A'_{trans} (blue) of a FPI with a mirror distance l suitable to resolve either (a) the ZPL or (b) the PSB.

5. Planning and building a Fabry-Pérot interferometer

The FPI is scanned by continuously varying the mirror distance l with a certain stepsize Δl and measuring the output-photon-flux every time. This process is sketched in figure 5.11. Similar to figure 5.10a the PSB can not be seen, as it is too weak to be visible in the linear scale.

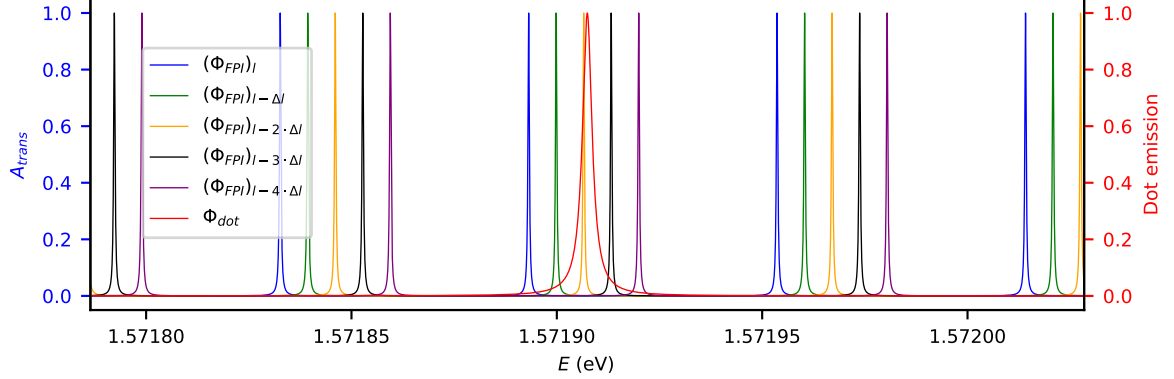


Figure 5.11.: Transmissions of the FPI modes A'_{trans} (blue) for different mirror distances $l - m \cdot \Delta l$ with $m \in \mathbb{N}$ compared to the exciton emission $\Phi_{dot}(E)$ (red).

The unnormalized output-photon-flux of the scanning FPI is then described with the convolution of $\Phi_{dot}(E)$ and $A'_{trans}(E)$

$$\tilde{\Phi}_{FPI}(E) = \int_{E_0-n\Delta}^{E_0+n\Delta} \Phi_{dot}(E') A'_{trans}(E - E') dE' \quad (5.64)$$

with E_0 as the central energy of the exciton emission line, Δ as the free spectral range and $2n = 4$ as the number of Airy peaks considered for the numerical convolution.

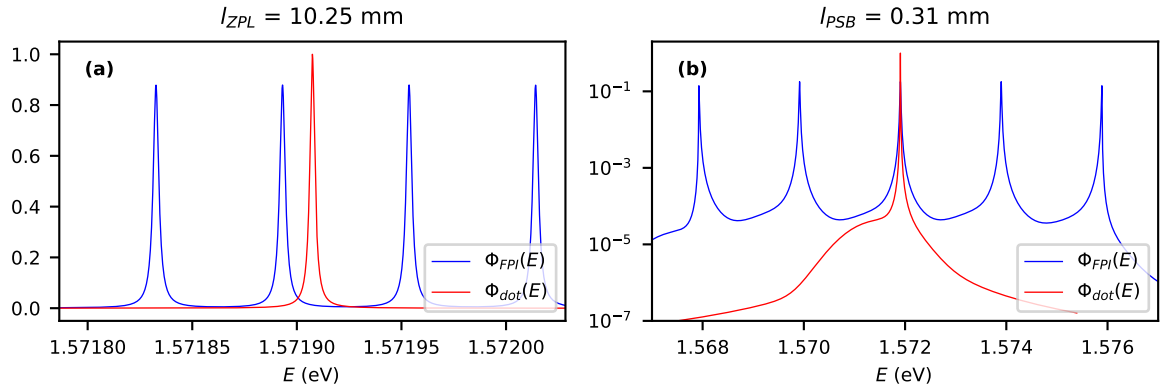


Figure 5.12.: Output-photon-flux of the scanning FPI $\Phi_{FPI}(E)$ (blue) compared to the exciton emission $\Phi_{dot}(E)$ (red) for (a) ZPL and (b) PSB.

$\tilde{\Phi}_{FPI}(E)$ can then be normalized with the integral of $A'_{trans}(E)$ over the same range

$$\Phi_{FPI}(E) = \frac{\tilde{\Phi}_{FPI}(E)}{\int_{E_0-n\cdot\Delta}^{E_0+n\cdot\Delta} A'_{trans}(E) dE} \quad (5.65)$$

A comparison of $\Phi_{FPI}(E)$ and $\Phi_{dot}(E)$ is shown in figure 5.12.

From now on, only the ZPL-path is shown as no new information is gained by examining both. In order to estimate the accuracy of the scanning FPI, the FPI modes are shifted by ΔE in order to overlap with $\Phi_{dot}(E)$ as depicted in figure 5.13a

$$\bar{\Phi}_{FPI}(E) = \Phi_{FPI}(E - \Delta E). \quad (5.66)$$

Afterwards, the absolute difference between those two $|\Phi_{dot}(E) - \bar{\Phi}_{FPI}(E)|$ is calculated as shown in figure 5.13b. Now the relative error of $\Phi_{fabry,perot}(E)$ for the given parameters and compared to the actual excitonic QD emission can be calculated

$$\epsilon = \frac{\int_{E_0-\Delta/2}^{E_0+\Delta/2} |\bar{\Phi}_{FPI}(E) - \Phi_{dot}(E)| dE}{\int_{E_0-\Delta/2}^{E_0+\Delta/2} \Phi_{dot}(E) dE} \quad (5.67)$$

For the parameters in the ZPL path this gives $\epsilon_{ZPL} = 10.57\%$.

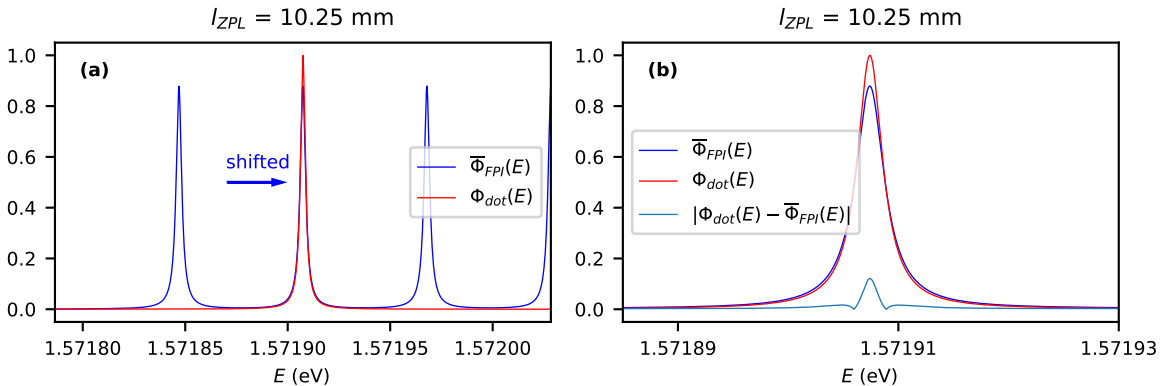


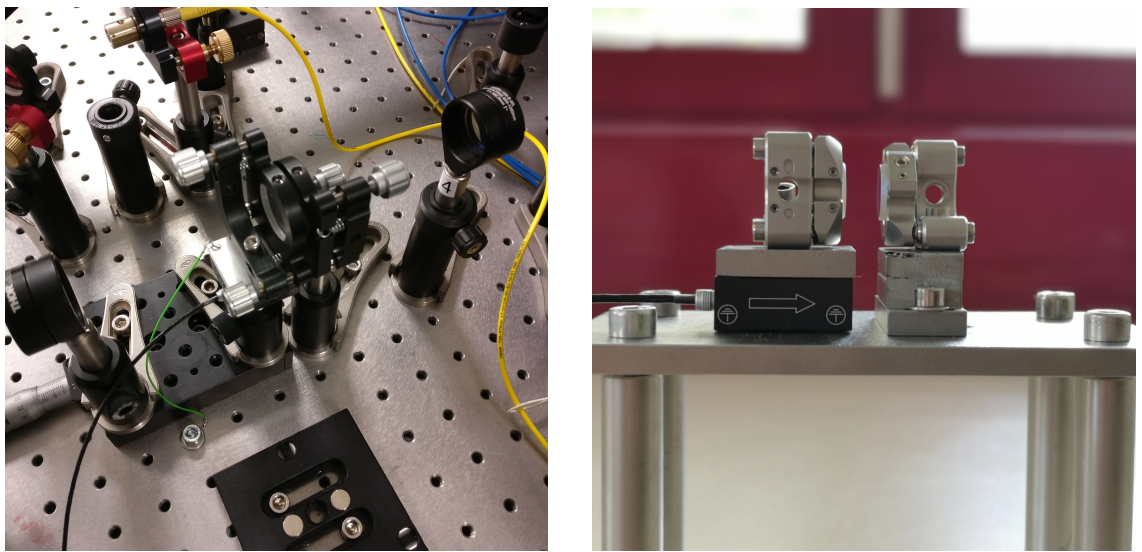
Figure 5.13.: In (a) the shifted output-photon-flux of the scanning FPI $\bar{\Phi}_{FPI}(E)$ (blue) compared to the exciton emission $\Phi_{dot}(E)$ (red) is displayed. In (b) the absolute difference between those two $|\bar{\Phi}_{FPI}(E) - \Phi_{dot}(E)|$ (light blue) is additionally shown.

5.5. Setup and testing

Multiple FPI setups were built up in order to test their suitability to resolve QD emission. The first version shown in figure 5.14a featured planar (diameter $d = 25.4$ mm) mirrors, while their distance

5. Planning and building a Fabry-Pérot interferometer

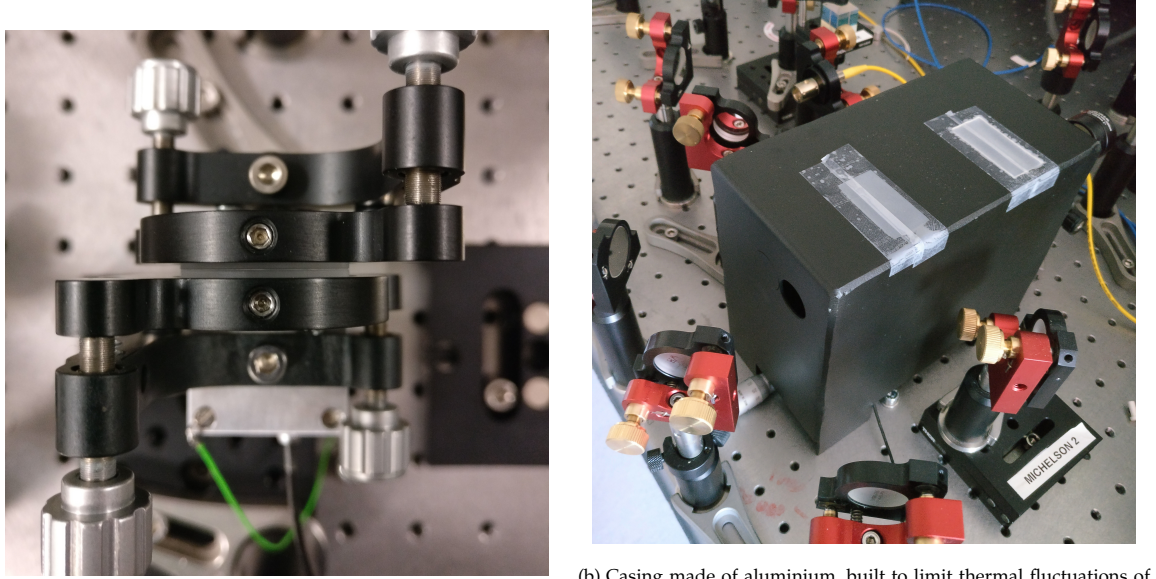
was coarsely tunable with an adjustable platform and finely tunable with a piezoelectrical actuator. It used a lens in order to minimize the spot size at the FPI and a second lens with the same focal length in order to restore the original spot size. The mirror-distances in figure 5.15a are in the order of sub-micrometer. This makes it difficult to ensure parallelism of the mirrors and also to estimate the mirror distances beforehand. In figure 5.15b, a casing is shown, built to block thermal fluctuations of the FPIs environment. However, these measures proved to be not sufficient as the setup with planar mirrors turned out to be highly unstable.



(a) FPI on adjustable platform and finely tunable with a piezoelectrical actuator and planar mirrors of diameter $d = 25.4$ mm.
 (b) FPI on molybdenum plate, coarsely tunable with elongated hole and finely tunable with a piezoelectrical actuator and planar mirrors of diameter of $d = 12.7$ mm.

Figure 5.14.: Comparison between two setups where one uses bigger, planar mirrors and one uses smaller, planar-convex mirrors

The second version shown in figure 5.14b used smaller ($r = 6.35$ mm), planar-convex mirrors and a ground plate made of molybdenum. Convex mirrors were implemented to allow mode-matching of the incoming beam. Molybdenum has a low thermal expansion coefficient, which is advantageous because of the FPI's sensitivity to mirror-distance-changes. This resulted in a stable FPI which was also adjustable for various free-spectral ranges. The measurements discussed in section 5.6 are obtained with this setup. However, the effort needed to mode-match for every measurement is too large to actually use it in further experiments. That is why the confocal setup will be used in the future, even though the freedom to adjust the free-spectral range is lost.



(a) Top view of FPI with planar mirrors.

(b) Casing made of aluminium, built to limit thermal fluctuations of the FPIs environment.

Figure 5.15.: Top view of FPI and casing.

5.5.1. Scanning mode with fast photodiodes

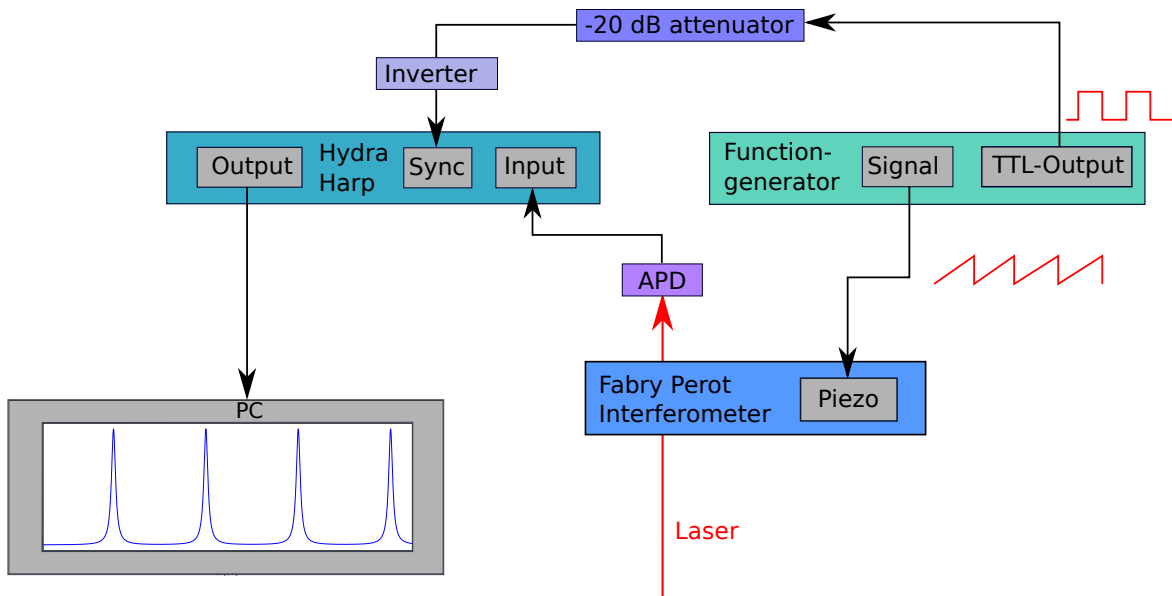


Figure 5.16.: Live avalanche photodiode setup using a function generator driving the piezo actuator of the FPI and the sync input of the correlation hardware. APDs are used because of their speed, allowing to live-adjusting the FPI-parameters.

5. Planning and building a Fabry-Pérot interferometer

Before the scanning FPI can be used to measure QD emission, it has to be aligned first usually with a (HeNe) laser. APDs are used for aligning the FPI as they are fast enough to measure the multiple free spectral ranges with a scanning frequency in the order of Hz. A function generator is used to drive the piezoelectrical actuator and the correlation hardware (here: Picoquant Hydralarp 400) correlates the measurements of the APD with the TTL-output of the function generator in the time domain. In order to do that the TTL-output has to be converted to the NIM standard beforehand, as this is the only one our correlation hardware accepts. TTL interprets 0 V as LOW and 5 V as HIGH and NIM interprets 0 V as LOW and negative values not lower than -1 V as HIGH. The conversion therefore involves inversion and attenuation of the signal. The complete setup is sketched in figure 5.16.

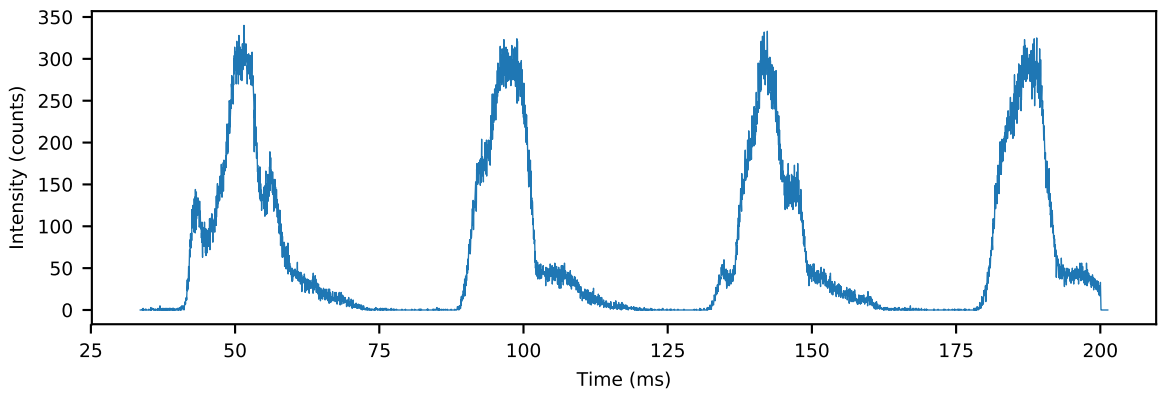


Figure 5.17.: Measurement of scanning FPI with APDs. The scanning frequency is 5 Hz and the range is 1 μm . The measured finesse is ≈ 5 and the free spectral range corresponds to 280 nm.

Figure 5.17 shows the measurement of the scanning FPI with the APDs. The scanning frequency is 5 Hz and the scanning distance is 1 μm . The measured finesse is approximately 5 and the free spectral range corresponds to 280 nm. The stability for one snapshot as visible here appears good, however the modes shift visibly over a longer period of time.

5.5.2. Scanning mode with CCD

In order to obtain the line shape of the input signal, the FPI is used in the scanning mode. The FPI is aligned with APDs and a HeNe laser as the former offers direct feedback and the latter emits visible light simplifying the procedure. Afterwards, the signal of interest will be measured, in our case QD emission. The piezoelectric actuator moves step-wise one of the mirrors and after every step the

output is recorded with the charge-coupled device (CCD). A minimal sketch of the setup is visible in figure 5.18.

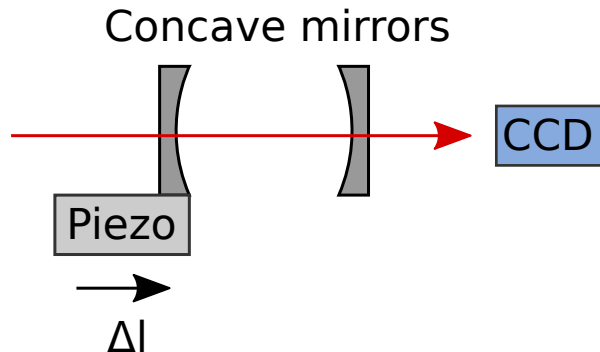


Figure 5.18.: Scanning Fabry Pérot interferometer with CCD

5.6. Measurements and discussion

In the following measurements the FPI was set up in the non-confocal mode and HeNe laser signals were used in order to align it. This involves positioning the laser beam so that it goes straight and centred through the FPI mirrors. Afterwards, the FPI mirrors are adjusted so that they are parallel and a single laser beam emerges as shown in figure 5.19.

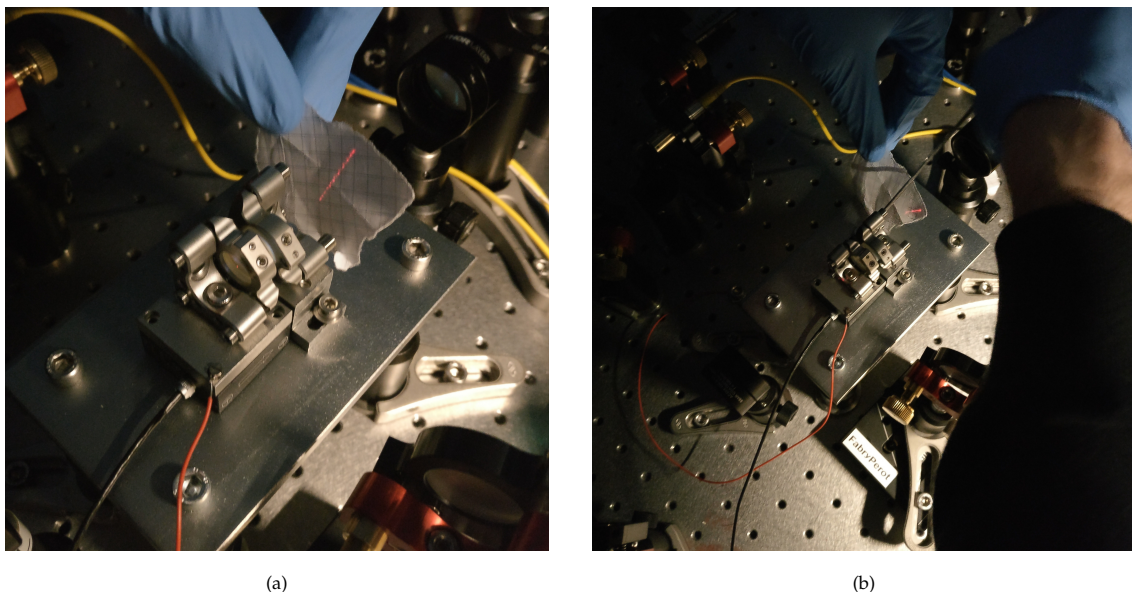


Figure 5.19.: Aligning the Fabry Pérot interferometer

5. Planning and building a Fabry-Pérot interferometer

Without spatial restriction strong TEM-modes of higher order are visible in figure 5.20a. To counteract them, a pinhole is inserted and adjusted, which results in the measurement visible in figure 5.20b. The intensity with and without FPI were compared in order to calculate the FPI's transmission at the peak of its modes, leading to $T_{peak} = 5\%$. With figure 5.20b the finesse can be calculated. As the mirror reflectivities $R = R_1 = R_2 = 97\%$, the mirror reflectivity finesse is $F = 155$. The measured finesse is 45 and obviously much lower. This is because the measured finesse F_t also depends on the mirror surface quality finesse F_q and the finesse due to illumination conditions (beam alignment and diameter) of the mirrors F_i as described by [52]

$$1/F_t = \left[(1/F)^2 + (1/F_q)^2 + (1/F_i)^2 \right]^{1/2}. \quad (5.68)$$

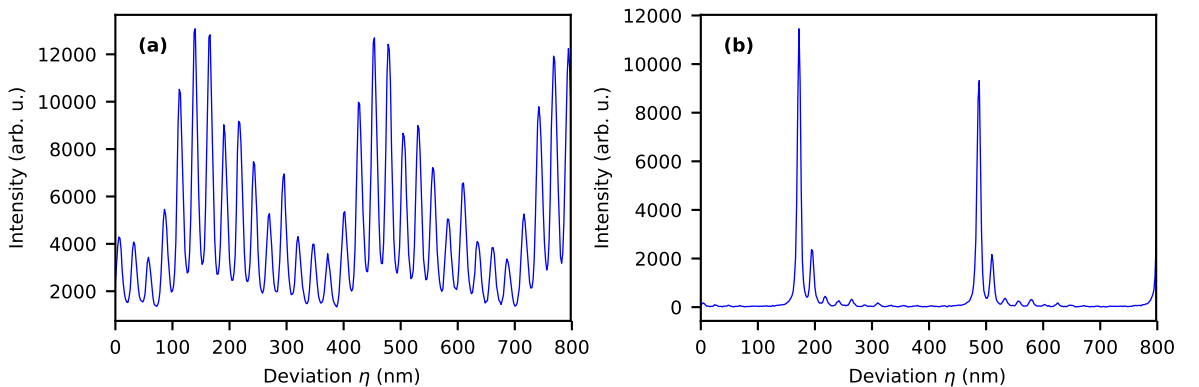


Figure 5.20.: Transmission measurement of FPI with ground mirror distance $l \approx 2$ mm and HeNe laser. (a) was aligned without spatial filtering with a pinhole and (b) involved a pinhole.

As can be seen in figure 5.20 the arrangement is stable enough that Cauchy peaks are symmetric and not distorted and fine details like the higher modes are resolvable. The temperature shift can be estimated under consideration of the expansion of the molybdenum-based groundplate. The coefficient of linear thermal expansion at room temperature of molybdenum is 5.2×10^{-6} m/(mK). This means that the shift for a mounting distance of the mirror holders of ≈ 50 mm is 260 nm/K. As a change of $\lambda/2$ in the mirror separation corresponds to a mode shift of one free spectral range, the corresponding FPI mode shift can be estimated. While measuring the excitonic emission of a GaAs QD of $\lambda_X = 785$ nm, a temperature change of 1 K would result in a FPI mode shift of 66.24 % of one free spectral range. It is therefore necessary to use a casing and to let the temperature stabilize before the measurement. However, it is empirically stable enough to conduct measurements which last shorter than 1 h.



Figure 5.21.: Polarization map of exciton-groundstate decay emission of QD in sample AS208. The peak to peak amplitude corresponds to the fine structure splitting.

Set up like this, the GaAs QD sample AS208 was measured. First, a polarization map of an exciton was recorded in order to determine the FSS. This works by putting a $\lambda/2$ -plate followed by a fixed linear polarizer between the QD and the spectrometer. The $\lambda/2$ -plate gets step-wisely rotated and the output will be recorded after every step. Because of the FSS of the QD, the recorded centre energy of the exciton-groundstate emission will shift after every step resulting in the plot shown in figure 5.21. The peak-to-peak amplitude then gives $E_{FSS} = 24.42(39)$ μeV .

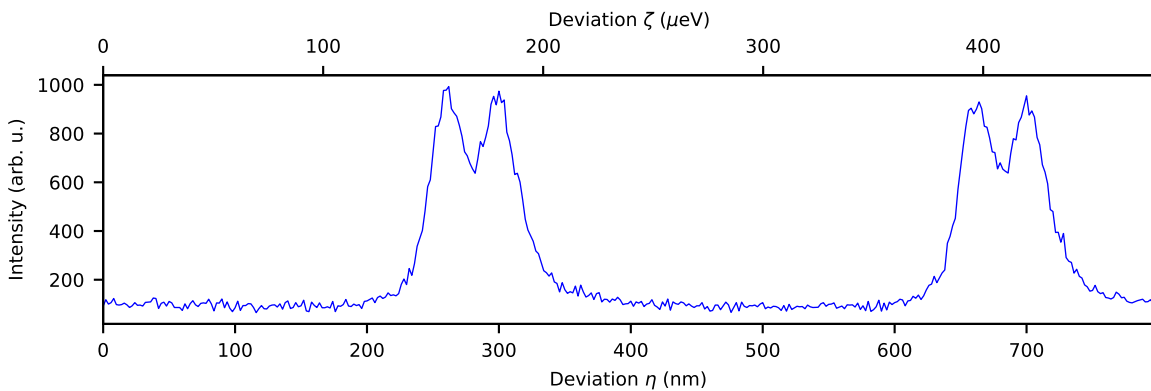


Figure 5.22.: Fine-structure measurement of exciton decay emission of a QD in sample AS208. It is measured by passing the QD emission through a FPI and sweeping the mirror distance. The ground mirror distance is $l \approx 2$ mm.

Afterwards, the output of the QD through the FPI was measured while the mirror distance was stepwisely changed as shown in figure 5.22. The two peaks per period display the splitted exciton-groundstate emission because of the FSS. As the distance between the peaks E_{FSS} was calculated

5. Planning and building a Fabry-Pérot interferometer

beforehand it is possible to convert the x-scale on the bottom in nm into the x-scale on the top in μeV . For this QD, it results in a conversion between the deviations of $\eta = 1 \text{ nm} \hat{=} \zeta = 1.19(2) \mu\text{eV}$. This gives a measured free spectral range of $241(4) \mu\text{eV}$ which is in the same order of the (coarsely) estimated mirror distance $l \approx 2 \text{ mm}$ free spectral range of $315 \mu\text{eV}$. In contrast to measurements with the HeNe-laser in figure 5.20, the higher transverse modes are not visible in figure 5.22. This is because there are two lines overlapping and the linewidth of a single one is already broader than the HeNe laser linewidth. Therefore, the higher transverse modes are overlaid by the fundamental mode.

From the performed measurements and the considerations about the stability, it can be deduced that with mirrors of correct geometry fine details of QD emission can be resolved. In order to use this in daily measurements however, mirrors with different curvature radii will be used in order to set up the FPI in order to satisfy the confocal conditions. This would liberate from time-consuming and error-prone mode-matching and spatial filtering.

6. Summary and outlook

This thesis describes the efforts to improve excitation of quantum dots (QDs) and to build up a scanning Fabry Pérot interferometer which allows to resolve fine details of QD emission spectra. In order to excite the QD via adiabatic rapid passage the chirp of the exciting laser beam needs to be deterministically adjustable. This again requires to build up a setup suitable to manipulate the chirp and a way to determine the chirp parameter α . The laser beam is measured with an interferometric auto correlator. However, the shape of this measurement depends only weakly on α . Therefore, the numerical filter MOSAIC is applied, which resulted in a signal of which the lower envelope depends strongly on α . The simulations show that a fit of the lower envelope of the MOSAIC signal allows to determine the chirp parameter. A pulse expander was built up, with the goal of deterministically adjusting the chirp by adapting the distance between two optical elements. Measurements with a Ti:Sa laser with and without a pulse expander were conducted, which suggested that the laser signal without the pulse expander is already heavily chirped. That is why future experiments will investigate different laser models and then compare the measurements with the chirped signal after the pulse expander. Additionally, the laser emission shape will be described more accurately in future simulations with a frequency comp instead of a simple Gaussian in order to better understand the influence of this approximation. Afterwards, QDs will be excited via adiabatic rapid passage. This topic was not continued, because the Ti:Sa laser had to undergo maintenance for several months which blocked further investigations.

The second topic of this thesis is the build-up of a scanning FPI. Simulations show that common optical components are sufficient to build up an FPI which is able to resolve the zero-phonon line of the QD emission. Measurements with planar mirrors show the instability of this arrangement, which is why we switched to planar-concave mirrors. The FPI is aligned with a HeNe laser and fast photodiodes, allowing to adjust the optical components of the FPI with direct feedback. Together with mode matching and spatial filtering, this allows to resolve the fine structure splitting of the excitonic energy levels of the QD. The transmission is determined to be 5 % and the thermal shift of the FPI

6. Summary and outlook

modes is estimated to be $\approx 66\%$ of one free spectral range per Kelvin. Both the transmission and the thermal drift are sufficient for resolving the splitted excitonic emission line. However, the measured finesse of 45 is too low to resolve near-Fourier-limited zero-phonon-lines. Also mode-matching and spatial-filtering is time consuming and error prone, which makes them impractical for common measurements. Therefore, the FPI is going to be used with mirrors of higher reflectivity and lower curvature radius and order to gain higher finesse and to use the FPI in the confocal mode. Here, the curvature radius is equal to the mirror distance, which removes the flexibility to change resolution and free spectral range of the FPI. However, the cavity becomes mode-degenerated and therefore liberates from mode matching considerations. The needed mirrors are already designed and ordered, however it was not possible to test the operation within the duration of this thesis.

Appendix

Appendix A.

Acronyms

QD	quantum dot	
FPI	Fabry P��rot interferometer	2
FSS	fine structure splitting	2
MBE	molecular beam epitaxy	3
CB	conduction band	3
VB	valence band	3
X	exciton	3
XX	biexciton	4
ZPL	zero phonon line	8
PSB	phonon side band	8
FCP	Franc-Condon principles	8
APD	avalanche photodiode	13
HBT	Hanbury-Brown-Twiss	12
BS	beam splitter	13
FWHM	full width at half maximum	16
MPL	micro photo-luminescence	16
ARP	adiabatic rapid passage	19
IAC	interferometric autocorrelation	22
MOSAIC	modified-spectrum autointerferometric correlation	23
CCD	charge-coupled device	51

Bibliography

- [1] Igor Aharonovich, Dirk Englund, and Milos Toth. "Solid-state single-photon emitters." In: *Nature Photonics* 10.10 (Oct. 2016), pp. 631–641. ISSN: 1749-4885, 1749-4893. DOI: 10.1038/nphoton.2016.186. URL: <http://www.nature.com/articles/nphoton.2016.186> (visited on 07/29/2019) (cit. on p. 1).
- [2] Jonathan P. Dowling and Gerard J. Milburn. "Quantum technology: the second quantum revolution." In: *Philosophical Transactions of the Royal Society of London. Series A: Mathematical, Physical and Engineering Sciences* 361.1809 (Aug. 15, 2003). Ed. by A. G. J. MacFarlane, pp. 1655–1674. ISSN: 1471-2962. DOI: 10.1098/rsta.2003.1227. URL: <http://www.royalsocietypublishing.org/doi/10.1098/rsta.2003.1227> (visited on 07/08/2019) (cit. on p. 1).
- [3] Anton Zeilinger. "Light for the quantum. Entangled photons and their applications: a very personal perspective." In: *Physica Scripta* 92.7 (July 1, 2017), p. 072501. ISSN: 0031-8949, 1402-4896. DOI: 10.1088/1402-4896/aa736d. URL: <http://stacks.iop.org/1402-4896/92/i=7/a=072501?key=crossref.0e8a32b86987e059b0432176f8f5b174> (visited on 07/26/2019) (cit. on p. 1).
- [4] Nicolas Gisin et al. "Quantum cryptography." In: *Reviews of Modern Physics* 74.1 (Mar. 8, 2002), pp. 145–195. ISSN: 0034-6861, 1539-0756. DOI: 10.1103/RevModPhys.74.145. URL: <https://link.aps.org/doi/10.1103/RevModPhys.74.145> (visited on 07/26/2019) (cit. on p. 1).
- [5] Artur K. Ekert. "Quantum cryptography based on Bell's theorem." In: *Physical Review Letters* 67.6 (Aug. 5, 1991), pp. 661–663. ISSN: 0031-9007. DOI: 10.1103/PhysRevLett.67.661. URL: <https://link.aps.org/doi/10.1103/PhysRevLett.67.661> (visited on 07/18/2019) (cit. on p. 1).
- [6] Nicolas Sangouard et al. "Quantum repeaters based on atomic ensembles and linear optics." In: *Reviews of Modern Physics* 83.1 (Mar. 21, 2011), pp. 33–80. ISSN: 0034-6861, 1539-0756. DOI: 10.1103/RevModPhys.83.33. URL: <https://link.aps.org/doi/10.1103/RevModPhys.83.33> (visited on 08/05/2019) (cit. on p. 1).

Bibliography

- [7] James L. Park. "The concept of transition in quantum mechanics." In: *Foundations of Physics* 1.1 (1970), pp. 23–33. ISSN: 0015-9018, 1572-9516. DOI: 10.1007/BF00708652. URL: <http://link.springer.com/10.1007/BF00708652> (visited on 07/29/2019) (cit. on p. 1).
- [8] Marcus Reindl et al. "All-photonic quantum teleportation using on-demand solid-state quantum emitters." In: *Science Advances* 4.12 (Dec. 2018), eaau1255. ISSN: 2375-2548. DOI: 10.1126/sciadv.aau1255. URL: <http://advances.sciencemag.org/lookup/doi/10.1126/sciadv.aau1255> (visited on 07/23/2019) (cit. on pp. 1, 2).
- [9] L.-M. Duan et al. "Long-distance quantum communication with atomic ensembles and linear optics." In: *Nature* 414.6862 (Nov. 2001), pp. 413–418. ISSN: 0028-0836, 1476-4687. DOI: 10.1038/35106500. URL: <http://www.nature.com/articles/35106500> (visited on 07/26/2019) (cit. on p. 1).
- [10] Christoph Simon et al. "Quantum Repeaters with Photon Pair Sources and Multimode Memories." In: *Physical Review Letters* 98.19 (May 11, 2007). ISSN: 0031-9007, 1079-7114. DOI: 10.1103/PhysRevLett.98.190503. URL: <https://link.aps.org/doi/10.1103/PhysRevLett.98.190503> (visited on 07/26/2019) (cit. on p. 1).
- [11] Y. H. Shih and C. O. Alley. "New Type of Einstein-Podolsky-Rosen-Bohm Experiment Using Pairs of Light Quanta Produced by Optical Parametric Down Conversion." In: *Physical Review Letters* 61.26 (Dec. 26, 1988), pp. 2921–2924. ISSN: 0031-9007. DOI: 10.1103/PhysRevLett.61.2921. URL: <https://link.aps.org/doi/10.1103/PhysRevLett.61.2921> (visited on 07/26/2019) (cit. on p. 2).
- [12] Bengt Nordén. "Entangled photons from single atoms and molecules." In: *Chemical Physics* 507 (May 2018), pp. 28–33. ISSN: 03010104. DOI: 10.1016/j.chemphys.2018.04.001. URL: <https://linkinghub.elsevier.com/retrieve/pii/S0301010418300648> (visited on 08/05/2019) (cit. on p. 2).
- [13] Alain Aspect, Philippe Grangier, and Gérard Roger. "Experimental Tests of Realistic Local Theories via Bell's Theorem." In: *Physical Review Letters* 47.7 (Aug. 17, 1981), pp. 460–463. ISSN: 0031-9007. DOI: 10.1103/PhysRevLett.47.460. URL: <https://link.aps.org/doi/10.1103/PhysRevLett.47.460> (visited on 07/26/2019) (cit. on p. 2).
- [14] Axel Kuhn, Markus Hennrich, and Gerhard Rempe. "Deterministic Single-Photon Source for Distributed Quantum Networking." In: *Physical Review Letters* 89.6 (July 19, 2002). ISSN: 0031-9007, 1079-7114. DOI: 10.1103/PhysRevLett.89.067901. URL: <https://link.aps.org/doi/10.1103/PhysRevLett.89.067901> (visited on 07/26/2019) (cit. on p. 2).

- [15] Jin Liu et al. "A solid-state source of strongly entangled photon pairs with high brightness and indistinguishability." In: *Nature Nanotechnology* 14.6 (June 2019), pp. 586–593. ISSN: 1748-3387, 1748-3395. DOI: 10.1038/s41565-019-0435-9. URL: <http://www.nature.com/articles/s41565-019-0435-9> (visited on 08/05/2019) (cit. on p. 2).
- [16] Lucas Schweickert et al. "On-demand generation of background-free single photons from a solid-state source." In: *Applied Physics Letters* 112.9 (Feb. 26, 2018), p. 093106. ISSN: 0003-6951, 1077-3118. DOI: 10.1063/1.5020038. URL: <http://aip.scitation.org/doi/10.1063/1.5020038> (visited on 08/05/2019) (cit. on p. 2).
- [17] Harishankar Jayakumar et al. "Deterministic Photon Pairs and Coherent Optical Control of a Single Quantum Dot." In: *Physical Review Letters* 110.13 (Mar. 26, 2013). ISSN: 0031-9007, 1079-7114. DOI: 10.1103/PhysRevLett.110.135505. URL: <https://link.aps.org/doi/10.1103/PhysRevLett.110.135505> (visited on 06/18/2019) (cit. on p. 2).
- [18] Daniel Huber. "GaAs quantum dots: A Dephasing-Free Source of Entangled Photon Pairs." PhD thesis. 2019 (cit. on pp. 3–5, 7, 11, 12).
- [19] Christian Schimpf. *Towards quantum teleportation with remote quantum dots*. 2017 (cit. on pp. 3, 7, 11–13, 15).
- [20] Zh. M. Wang et al. "Nanoholes fabricated by self-assembled gallium nanodrill on GaAs(100)." In: *Applied Physics Letters* 90.11 (Mar. 12, 2007), p. 113120. ISSN: 0003-6951, 1077-3118. DOI: 10.1063/1.2713745. URL: <http://aip.scitation.org/doi/10.1063/1.2713745> (visited on 06/13/2019) (cit. on p. 3).
- [21] Dieter Bimberg, Marius Grundmann, and Nikolai N. Ledentsov. *Quantum dot heterostructures*. Chichester, [Eng.]; New York: John Wiley, 1999. 328 pp. ISBN: 978-0-471-97388-1 (cit. on p. 3).
- [22] R. M. Stevenson et al. "A semiconductor source of triggered entangled photon pairs." In: *Nature* 439.7073 (Jan. 2006), pp. 179–182. ISSN: 0028-0836, 1476-4687. DOI: 10.1038/nature04446. URL: <http://www.nature.com/articles/nature04446> (visited on 06/17/2019) (cit. on p. 4).
- [23] M. Bayer et al. "Fine structure of neutral and charged excitons in self-assembled In(Ga)As/(Al)GaAs quantum dots." In: *Physical Review B* 65.19 (May 7, 2002). ISSN: 0163-1829, 1095-3795. DOI: 10.1103/PhysRevB.65.195315. URL: <https://link.aps.org/doi/10.1103/PhysRevB.65.195315> (visited on 06/17/2019) (cit. on p. 6).
- [24] E. Peter et al. "Phonon sidebands in exciton and biexciton emission from single GaAs quantum dots." In: *Physical Review B* 69.4 (Jan. 26, 2004), p. 041307. ISSN: 1098-0121, 1550-235X. DOI: 10.

Bibliography

- 1103/PhysRevB.69.041307. URL: <https://link.aps.org/doi/10.1103/PhysRevB.69.041307> (visited on 06/11/2019) (cit. on p. 8).
- [25] Antoine Reigue et al. "Probing Electron-Phonon Interaction through Two-Photon Interference in Resonantly Driven Semiconductor Quantum Dots." In: *Physical Review Letters* 118.23 (June 6, 2017). ISSN: 0031-9007, 1079-7114. DOI: 10.1103/PhysRevLett.118.233602. URL: <http://link.aps.org/doi/10.1103/PhysRevLett.118.233602> (visited on 07/23/2019) (cit. on p. 8).
- [26] Josef Friedrich and Dietrich Haarer. "Photochemical Hole Burning: A Spectroscopic Study of Relaxation Processes in Polymers and Glasses." In: *Angewandte Chemie International Edition in English* 23.2 (Feb. 1984), pp. 113–140. ISSN: 0570-0833, 1521-3773. DOI: 10.1002/anie.198401131. URL: <http://doi.wiley.com/10.1002/anie.198401131> (visited on 06/11/2019) (cit. on p. 8).
- [27] J. Franck and E. G. Dymond. "Elementary processes of photochemical reactions." In: *Transactions of the Faraday Society* 21 (February 1926), p. 536. ISSN: 0014-7672. DOI: 10.1039/tf9262100536. URL: <http://xlink.rsc.org/?DOI=tf9262100536> (visited on 07/22/2019) (cit. on p. 8).
- [28] *Zero-phonon line and phonon sideband - Wikipedia*. URL: https://en.wikipedia.org/wiki/Zero-phonon_line_and_phonon_sideband (visited on 06/11/2019) (cit. on p. 9).
- [29] Eva Schöll et al. "Resonance fluorescence of GaAs quantum dots with near-unity photon indistinguishability." In: *Nano Letters* 19.4 (Apr. 10, 2019), pp. 2404–2410. ISSN: 1530-6984, 1530-6992. DOI: 10.1021/acs.nanolett.8b05132. arXiv: 1901.09721. URL: <http://arxiv.org/abs/1901.09721> (visited on 05/09/2019) (cit. on p. 10).
- [30] Takashi Kuroda et al. "Symmetric quantum dots as efficient sources of highly entangled photons: Violation of Bell's inequality without spectral and temporal filtering." In: *Physical Review B* 88.4 (July 18, 2013). ISSN: 1098-0121, 1550-235X. DOI: 10.1103/PhysRevB.88.041306. URL: <https://link.aps.org/doi/10.1103/PhysRevB.88.041306> (visited on 06/18/2019) (cit. on p. 11).
- [31] Peter Michler, ed. *Single semiconductor quantum dots*. Nanoscience and technology. OCLC: ocn248993461. Berlin: Springer, 2009. 389 pp. ISBN: 978-3-540-87445-4 978-3-540-87446-1 (cit. on p. 11).
- [32] Marcus Reindl et al. "Phonon-Assisted Two-Photon Interference from Remote Quantum Emitters." In: *Nano Letters* 17.7 (July 12, 2017), pp. 4090–4095. ISSN: 1530-6984, 1530-6992. DOI: 10.1021/acs.nanolett.7b00777. URL: <http://pubs.acs.org/doi/10.1021/acs.nanolett.7b00777> (visited on 06/19/2019) (cit. on pp. 11, 12).

- [33] S. Stufler et al. "Two-photon Rabi oscillations in a single In x Ga $1 - x$ AsGa As quantum dot." In: *Physical Review B* 73.12 (Mar. 7, 2006). ISSN: 1098-0121, 1550-235X. DOI: 10.1103/PhysRevB.73.125304. URL: <https://link.aps.org/doi/10.1103/PhysRevB.73.125304> (visited on 06/19/2019) (cit. on p. 12).
- [34] J. Förstner et al. "Phonon-Assisted Damping of Rabi Oscillations in Semiconductor Quantum Dots." In: *Physical Review Letters* 91.12 (Sept. 16, 2003). ISSN: 0031-9007, 1079-7114. DOI: 10.1103/PhysRevLett.91.127401. URL: <https://link.aps.org/doi/10.1103/PhysRevLett.91.127401> (visited on 06/19/2019) (cit. on p. 12).
- [35] Jan-Philipp Jahn et al. "An artificial Rb atom in a semiconductor with lifetime-limited linewidth." In: *Physical Review B* 92.24 (Dec. 28, 2015). ISSN: 1098-0121, 1550-235X. DOI: 10.1103/PhysRevB.92.245439. URL: <https://link.aps.org/doi/10.1103/PhysRevB.92.245439> (visited on 08/05/2019) (cit. on p. 16).
- [36] Florian Sipek. *Spectral shaping of femto-second pulses for resonant two-photon excitation of semiconductor quantum dots*. 2016 (cit. on p. 16).
- [37] Marcus Reindl. *Characterisation of semiconductor quantum dots by means of advanced optical spectroscopy techniques*. 2014 (cit. on pp. 16, 17).
- [38] M. Glässl et al. "Biexciton state preparation in a quantum dot via adiabatic rapid passage: Comparison between two control protocols and impact of phonon-induced dephasing." In: *Physical Review B* 87.8 (Feb. 8, 2013). ISSN: 1098-0121, 1550-235X. DOI: 10.1103/PhysRevB.87.085303. URL: <https://link.aps.org/doi/10.1103/PhysRevB.87.085303> (visited on 05/13/2019) (cit. on pp. 20, 27).
- [39] Toshiyuki Hirayama and Mansoor Sheik-Bahae. "Real-time chirp diagnostic for ultrashort laser pulses." In: *Optics Letters* 27.10 (May 15, 2002), p. 860. ISSN: 0146-9592, 1539-4794. DOI: 10.1364/OL.27.000860. URL: <https://www.osapublishing.org/abstract.cfm?URI=ol-27-10-860> (visited on 05/13/2019) (cit. on pp. 20, 23).
- [40] *Optical autocorrelation - Wikipedia*. URL: https://en.wikipedia.org/wiki/Optical_autocorrelation (visited on 06/25/2019) (cit. on p. 22).
- [41] Jean-Claude Diels and Wolfgang Rudolph. *Ultrashort laser pulse phenomena: fundamentals, techniques, and applications on a femtosecond time scale*. 2nd ed. Optics and photonics. Amsterdam ; Boston: Elsevier / Academic Press, 2006. 652 pp. ISBN: 978-0-12-215493-5 (cit. on p. 22).
- [42] Miles V. Klein and Thomas E. Furtak. *Optics*. 2nd ed. New York: Wiley, 1986. 660 pp. ISBN: 978-0-471-87297-9 (cit. on p. 24).

Bibliography

- [43] O. Martinez. “3000 times grating compressor with positive group velocity dispersion: Application to fiber compensation in 1.3-1.6 um region.” In: *IEEE Journal of Quantum Electronics* 23.1 (Jan. 1987), pp. 59–64. ISSN: 0018-9197. DOI: 10.1109/JQE.1987.1073201. URL: <http://ieeexplore.ieee.org/document/1073201/> (visited on 06/28/2019) (cit. on pp. 25, 26).
- [44] Sophocles J. Orfanidis. *Electromagnetic waves and antennas*. 2002 (cit. on p. 26).
- [45] V.S. Malinovsky and J.L. Krause. “General theory of population transfer by adiabatic rapid passage with intense, chirped laser pulses.” In: *The European Physical Journal D* 14.2 (May 2001), pp. 147–155. ISSN: 14346060. DOI: 10.1007/s100530170212. URL: <http://www.springerlink.com/index/10.1007/s100530170212> (visited on 07/22/2019) (cit. on p. 27).
- [46] Timo Kaldewey et al. “Coherent and robust high-fidelity generation of a biexciton in a quantum dot by rapid adiabatic passage.” In: *Physical Review B* 95.16 (Apr. 10, 2017). ISSN: 2469-9950, 2469-9969. DOI: 10.1103/PhysRevB.95.161302. arXiv: 1701.01371. URL: <http://arxiv.org/abs/1701.01371> (visited on 12/11/2018) (cit. on p. 31).
- [47] Dieter Meschede. *Optik, Licht und Laser*. 3., durchges. Aufl. Studium. OCLC: 254422596. Wiesbaden: Vieweg + Teubner, 2008. 568 pp. ISBN: 978-3-8351-0143-2 (cit. on pp. 31, 33, 40, 43).
- [48] Nur Ismail et al. “Fabry-Pérot resonator: spectral line shapes, generic and related Airy distributions, linewidths, finesse, and performance at low or frequency-dependent reflectivity.” In: *Optics Express* 24.15 (July 25, 2016), p. 16366. ISSN: 1094-4087. DOI: 10.1364/OE.24.016366. URL: <https://www.osapublishing.org/abstract.cfm?URI=oe-24-15-16366> (visited on 05/13/2019) (cit. on pp. 35, 37).
- [49] *Fabry-Pérot interferometer - Wikipedia*. URL: https://en.wikipedia.org/wiki/Fabry%25E2%2580%2593%C3%A9rot_interferometer (visited on 05/06/2019) (cit. on pp. 37–39).
- [50] Amnon Yariv, Pochi Yeh, and Amnon Yariv. *Photonics: optical electronics in modern communications*. 6th ed. The Oxford series in electrical and computer engineering. OCLC: ocm58648003. New York: Oxford University Press, 2007. 836 pp. ISBN: 978-0-19-517946-0 (cit. on p. 40).
- [51] Michael Hercher. “The Spherical Mirror Fabry-Perot Interferometer.” In: *Applied Optics* 7.5 (May 1, 1968), p. 951. ISSN: 0003-6935, 1539-4522. DOI: 10.1364/AO.7.000951. URL: <https://www.osapublishing.org/abstract.cfm?URI=ao-7-5-951> (visited on 05/09/2019) (cit. on p. 43).
- [52] *Scanning Fabry-Perot Interferometers*. URL: https://www.thorlabs.com/newgroupage9.cfm?objectgroup_ID=859 (visited on 08/05/2019) (cit. on p. 52).